DEUTSCHES ELEKTRONEN-SYNCHROTRON DESY
DESY 84-006
January 1984

受入
84-3-15
物理図書室

ON THE NUMERICAL SOLUTION OF MAXWELL'S EQUATIONS AND APPLICATIONS IN THE FIELD OF ACCELERATOR PHYSICS

by

T. Weiland
Deutsches Elektronen-Synchrotron DESY, Hamburg

ISSN 0418-9833

NOTKESTRASSE 85 · 2 HAMBURG 52

DESY behält sich alle Rechte für den Fall der Schutzrechtserteilung und für die wirtschaftliche Verwertung der in diesem Bericht enthaltenen Informationen vor.

DESY reserves all rights for commercial use of information included in this report, especially in case of filing application for or grant of patents.

To be sure that your preprints are promptly included in the HIGH ENERGY PHYSICS INDEX , send them to the following address (if possible by air mail) :

DESY
Bibliothek
Notkestrasse 85
2 Hamburg 52
Germany

Thomas Weiland
DESY
Notkestraße 85

2000 Hamburg 52

DESY 84-006
January 1984

ISSN 0418-9833

On the Numerical Solution of Maxwell's Equations and applications in the field of accelerator physics

Abstract

A discretization ansatz for Maxwell's equations is described that enables treatment of all possible homogeneous and inhomogeneous problems from nonlinear magnetostatics and electrostatics to time dependent field problems which include charges moving freely at any speed. One and the same method can be used for magnet design, for cavity mode investigations and wake force computations in time and frequency domain, antenna problems and waveguide structures.

The method makes direct use of the electric or/and magnetic field as unknowns thus yielding uniquely defined vectors in combination with a suitable grid definition. This "natural" ansatz avoids problems arising from the use of artificial functions such as vector potentials or Hertz potentials.

Using this ansatz, many computer codes have been developed and applied to various problems. Applications in the field of accelerator physics include magnet and solenoid design; design of accelerating rf-cavities and beam tracking calculations for instability studies. More recently the method has been used to study the new acceleration principle of wake field compression.

Contents

Glossary

A	Area of integration
(A)	Border of A
$\vec{E}$	Electric field vector
$\vec{D}$	Electric flux density vector, $\vec{D} = \varepsilon \cdot \vec{E}$
$\vec{H}$	Magnetic field vector
$\vec{B}$	Magnetic flux density vector
$\vec{J}$	Current density vector, $\vec{J} = \gamma\vec{E}$
V	Volume of integration
(V)	Surface of V
γ	Conductivity (tensor), mass in units of the rest mass
ε	Permittivity (tensor)
$\underline{\varepsilon}$	Complex permittivity (tensor), $\underline{\varepsilon} = \varepsilon_r(1 - i \tan\delta)$
i	$\sqrt{-1}$
δ	Loss angle of a dielectric
μ	Permeability (tensor)
ω	Circular frequency
$\underline{\vec{x}}$	Complex phasor, $\vec{x}(t) = \mathrm{Re}\{\underline{\vec{x}} \cdot \exp(i\omega t)\}$ $\vec{x} = \vec{E}, \vec{H}, \vec{D}, \vec{B}$ or $\vec{J}$
$\underline{\vec{J}}_e, \underline{\vec{J}}_d$	Phasor of eddy current density/driving current density
$\underline{k}(\omega)$	Complex propagation constant, $\underline{k}(\omega) = \beta(\omega) - i\alpha(\omega)$
k_o	Wave number, $k_o = \omega/c_o$
ρ	Charge density
λ	Line charge density
Q	Charge
$\vec{v}$	Velocity
β	$\lvert\vec{v}\rvert$ in units of c_o / phase constant of waveguide

c_o	Speed of light in vacuum
i, j, k	Running index for mesh line coordinates
I, J, K	Number of grid lines in the three spatial directions
n	Running index for grid nodes, $n = i + (j - 1) \cdot I + (k - 1) \cdot I \cdot J$
N	Total number of grid nodes, $N = I \cdot J \cdot K$
$\vec{e}, \vec{h}, \vec{d}, \vec{b}$	Column vector of dimension N...3N holding all unknown electric /magnetic field/flux density components in the grid
$\vec{g}$	Column vector of the total current components
$\vec{\varphi}$	Vector holding all unknown potentials at the grid nodes
ϕ	Potential
$\vec{c}$	Short for right hand side vector in matrix equations
$O(\Delta)$	Landau symbol
$d\vec{s}, d\vec{A}, dV$	Path, area and volume element
$D_{\varepsilon, \mu, \gamma}$	Diagonal matrices representing material properties
$D^{1/2}$	Diagonal matrix with $(D^{1/2})_{ii} = \sqrt{(D)_{ii}}$
$R, \tilde{R}$	"curl" operators in the grid G, $\tilde{G}$
$W_{\parallel}(s)$	Green's function for the longitudinal wake potential
$W_{\perp}(s)$	Green's function for the transverse wake potential
T_o	Revolution time in a storage ring
T_ε	Energy oscillation damping time
α	Momentum compaction factor/damping rate of waveguide
$\sigma_{o\varepsilon}$	rms energy spread
U_{syn}	Synchrotron radiation loss per turn
Q_{tot}	total charge in a bunch

1 Introduction

The unified theory of electric and magnetic fields is described by Maxwell's equations[1]:

$$(1) \qquad \oint_{(A)} \vec{E} \cdot d\vec{s} = - \iint_{A} \frac{\partial \vec{B}}{\partial t} \cdot d\vec{A}$$

$$(2) \qquad \oint_{(A)} \vec{H} \cdot d\vec{s} = \iint_{A} \left(\frac{\partial \vec{D}}{\partial t} + \vec{J} + \rho\vec{v}\right) \cdot d\vec{A}$$

$$(3) \qquad \iint_{(V)} \vec{B} \cdot d\vec{A} = 0$$

$$(4) \qquad \iint_{(V)} \left(\frac{\partial \vec{D}}{\partial t} + \vec{J} + \rho \cdot \vec{v}\right) \cdot d\vec{A} = 0$$

In these equations $\vec{E}$ and $\vec{H}$ are the electric and magnetic field and $\vec{D}$ and $\vec{B}$ are the electric and magnetic flux densities. The current density is denoted by $\vec{J}$ whereas ρ denotes the charge density. The fields and the flux densities are related by:

$$(5) \qquad \vec{D} = \varepsilon\vec{E} \ ,$$

$$(6) \qquad \vec{B} = \mu\vec{H} \ ,$$

whereas the current density is given by Ohm's law:

$$(7) \qquad \vec{J} = \gamma\vec{E} \ .$$

The three material functions ε, μ and γ (permittivity, permeability and conductivity) are in general functions of the spatial coordinates and also nonlinear functions of the electromagnetic field strength, e.g. saturation effects in metal. All three material properties may be tensors. (We leave out here the hysteresis effect).
The excitation term in Maxwell's equations is given by $\rho \cdot \vec{v}$ or by a prescribed current density $\vec{J}_d$ (d for driving).
The ultimate goal in solving Maxwell's equations is to find a method that includes realisticely shaped structures and material distributions in two and three dimensions. Furthermore such a method should be applicable to a variety of problems such as electrostatic fields, magnetostatic fields, static current flow problems, eddy currents in laminated and solid metallic bodies, high frequency waveguides and resonators, antenna radiation and time dependent fields of clouds of charges moving freely at any speed.

The usual procedure of attacking these problems is to simplify the equations as far as possible (e.g. setting some of the quantities ε, μ or γ as constant) and to deduce from Maxwell's equations a second order differential equation. This second order differential equation for some intermediate function (e.g. a vector potential, scalar potential or both) can then be solved - for realisticly shaped structures - by means of finite difference, finite element or integral methods.
The aim of this paper is to describe a method that solves directly Maxwell's equations (1)-(4) in integral form. Instead of introducing intermediate functions - e.g. potentials - we follow the suggestion to use directly the electromagnetic field or flux densities[2]- except for static problems - and we derive the generalized finite integration theory[3](FIT). Consequently the solutions are uniquely defined (by the physics) and boundary conditions as well as transition conditions between areas of different material are readily verified in a natural way. The FIT method is applicable under very general conditions as far as material distributions are concerned. Only one single ansatz is needed to address the whole variety of problems listed above.

2. Theory

2.1 The general FIT method

As a starting point we consider two realistic examples shown in figures 1 and 2. Figure 1a shows a (three dimensional) dipole bending magnet and figure 2a a double microstrip transmission line on a dielectric support surrounded by a rectangular metallic waveguide structure. In order to represent such geometries we will use throughout this paper "rectangular" orthogonal - not necessarily cartesian - grids. Figures 1b and 2b show such grids with irregular step sizes. In many cases - as in the two examples shown here - the object of investigation has some symmetry properties thus allowing a reduction to a fraction of the original size for the calculations.
In general one can not expect the structures to be investigated to fit the grid lines exactly in an orthogonal coordinate system as happened in the case of the two first examples. Therefore any non fitting area (volume) has to be approximated by structures consisting of mesh cells as smallest units. Here we find a first possible source of error in the calculated results. A typical problem is shown in figure 3: a circular curve - which may be the boundary of any material - has to be represented in a rectangular mesh.

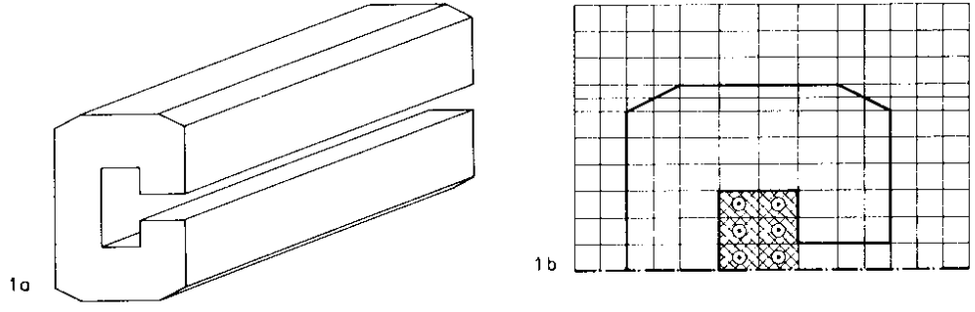

Figure 1: C-shaped dipole bending magnet (a) and course mesh for representing its cross section (b) using triangular sub cells and exploiting the symmetries

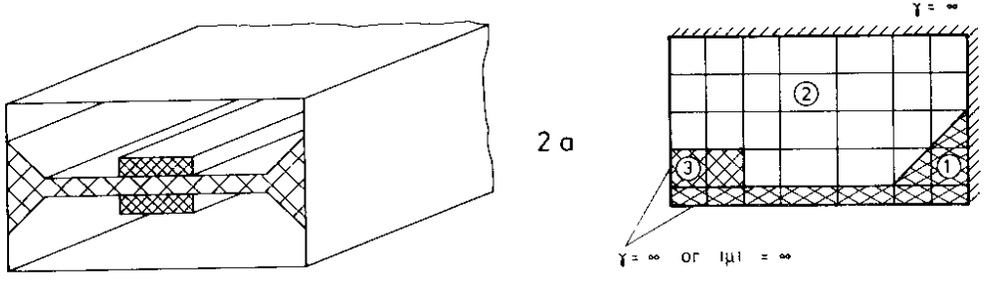

Figure 2: Double micro strip transmission line on dielectric support in a metallic rectangular waveguide (a) and course mesh representing a quarter of its cross section (b). Material (1) is dielectric, (2) vacuum and (3) may be either dielectric or metal

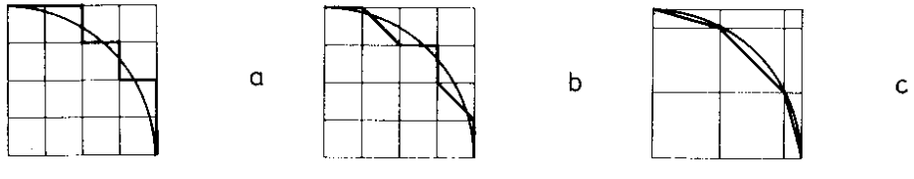

Figure 3: Three possible approximations to a circular shape in a mesh
a) usual "stair step" approximation
b) extended triangular sub cell approximation
c) extended triangular sub cells combined with irregular mesh steps

Figure 3a shows the usual approach of stair step approximation. Figure 3b gives an improved representation in the same regular mesh by means of triangles that further subdivide a rectangular mesh cell. A combination of triangular sub cells and irregular mesh steps obviously enables much better approximations with even fewer grid lines as demonstrated in figure 3c. (This example is used just for demonstration and it is clear that a regular r-φ cylindrical mesh would be much more suitable.)

In the following we will allow a different kind of material (ε, μ and γ) in each mesh cell. Each cell may be further divided into triangular sub cells (or prisms/tetrahedrons in three dimensional cases). Thus with a given grid and material constants allocated to each cell the geometry of the problem is defined.

The next step will be to solve Maxwell's equations in these mesh approximations taking into account the material distribution plus boundary conditions at the border of the grid. In the first Maxwell's equation we find two different types of integrals, a line integral along the circumference of an area and an integral over the enclosed area. Starting with the line integral we will try to use the most simple numerical integration technique, see figure 4:

$$(8) \qquad \int_{x_0}^{x_0+\Delta} f(x)\,dx = \Delta \cdot f(x_0 + \tfrac{\Delta}{2}) + O(\Delta)^2 \ .$$

In order to apply the above formula to the left hand side of Eq. (1) we have to define the areas of integration. The obvious choice is to use the cells as smallest units. Hence the direction of $\vec{ds}$ is defined as parallel to the grid lines. Scalar products - as they occur here ($\vec{E} \cdot \vec{ds}$) - are eliminated by representing $\vec{E}$ only by the component that has the same direction as $\vec{ds}$ as shown in figure 5. Finally the left hand side of Maxwell's first equations is simply approximated by:

$$(9) \qquad \oint_{(\text{cell})} \vec{E} \cdot \vec{ds} = E_1 \cdot \Delta + E_2 \cdot \Delta - E_3 \cdot \Delta - E_4 \cdot \Delta + O(\Delta)^2 \ .$$

Note that this natural allocation implied by Maxwell's equations in integral form yields different components of the field represented at different locations in the grid (e.g. in figure 5 E_1 and E_3 are horizontal components and E_2, E_4 are vertical components).

In practice we will always use irregular grids but for this introduction we want to avoid unnecessary indices and use a constant mesh step size Δ in all directions.

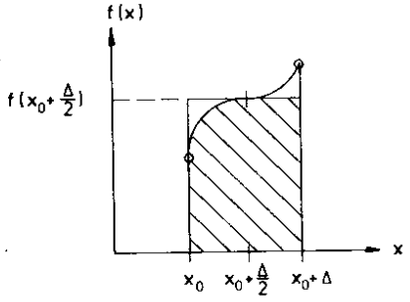

Figure 4: Simplest numerical approximation for one dimensional line integrals

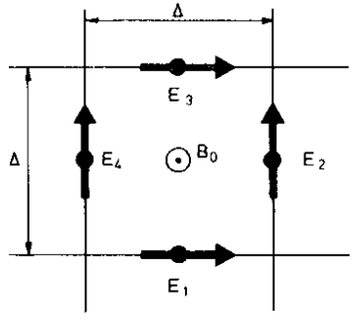

Figure 5: Single mesh cell with four electric field components allocated around the circumference and one component of the magnetic flux density allocated to the middle of and perpendicular to the cell area

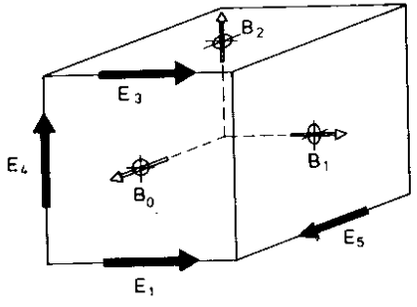

Figure 6: Three dimensional view of a mesh cell showing the magnetic flux density components evaluated at the middle of and perpendicular to the cell surface areas

Now that the LHS of the first Maxwell's equation has been approximated we have to integrate the RHS over the enclosed area. Again we use the simplest integration formula known:

$$(10) \qquad \int_{x_0}^{x_0+\Delta} \int_{y_0}^{y_0+\Delta} f(x, y)\, dx\, dy = \Delta^2 \cdot f(x_0 + \tfrac{\Delta}{2};\ y_0 + \tfrac{\Delta}{2}) + O(\Delta^4)$$

Since the RHS of (1) contains a scalar product too we choose $\vec{B}$ in the same direction as $d\vec{A}$ and represent $\vec{B}$ only by its perpendicular component evaluated at the middle of the cell area, see fig. 5. We apply the above integration formula:

$$(11) \qquad \iint_{\text{cell}} \frac{\partial}{\partial t} \vec{B} \cdot d\vec{A} = \Delta^2 \cdot \dot{B}_0 + O(\Delta^4)$$

Combining equ's (9) and (11) yields:

$$(12) \qquad \begin{array}{ccc} \oint_{(A)} \vec{E} \cdot d\vec{s} & = - & \iint_{A} \frac{\partial}{\partial t} \vec{B} \cdot d\vec{A} \\ \Downarrow & & \Downarrow \\ \Delta(E_1 + E_2 - E_3 - E_4) & = - & \Delta^2 \dot{B}_0 + O(\Delta^2) \end{array}$$

Now that we have fulfilled Maxwell's equation (1) for a single mesh cell we can satisfy this equation for any curve in the grid by a combination of many mesh cell equations.

Performing the above type of equation for all cells in the grid replaces the continuous vector functions $\vec{E}(\vec{r})$ and $\vec{B}(\vec{r})$ by a (large) number of the values of their components at given locations in the grid. In other words $\vec{E}(\vec{B})$ is replaced by a column vector $\vec{e}(\vec{b})$ of large dimension holding all the unknown components.

Figure 6 shows a 3D view of a single mesh cell and the magnetic flux components in the middle of the cell areas. Connection of these little vectors by new grid lines as shown in figure 7a (3D) and 7b (2D) generates a second grid which we name $\tilde{G}$.

In the newly defined "dual" or "magnetic" grid $\tilde{G}$ the magnetic flux density components are allocated in exactly the same way as are the electric field components in the "electric" grid G.

Since the material properties are different in each cell the question arises of whether the continuity equations for the tangential field components and for the perpendicular flux density components are fulfilled at material surfaces.

By setting up the grids and the field location inductively from the first Maxwell's equation both continuity equations are a priory satisfied as illustrated in figure 8. Since the electric field is represented only by tangential components and the magnetic flux density only by perpendicular ones there is no necessity for satisfying the continuity equations explicitly. Furthermore $\vec{E}$ and $\vec{B}$ are everywhere uniquely defined.

So far we have treated only the first one of Maxwell's equations. The second one (Eq. (2)) is very similar the main difference being that $\vec{E}$ and $\vec{B}$ are interchanged. Since the $\vec{B}$ components are located in $\tilde{G}$ as the $\vec{E}$ components are in G we can apply the same technique for approximating the integrals as we used for Eq. (1). Only a little complication arises from the fact that magnetic field $\vec{H}$ occurs in the equation but the flux density has been allocated to $\tilde{G}$. As can be seen from figure 9 we get:

(13)
$$\oint_{(A)} \vec{H} \cdot d\vec{s} = \iint_{A} \left(\varepsilon \frac{\partial \vec{E}}{\partial t} + \gamma \vec{E} + \rho \vec{v}\right) \cdot d\vec{A}$$

$$\left.\begin{aligned} &\frac{2\Delta}{\mu_1+\mu_2} B_1 + \frac{2\Delta}{\mu_2+\mu_3} B_2 + \\ &- \frac{2\Delta}{\mu_3+\mu_4} B_3 - \frac{2\Delta}{\mu_4+\mu_1} B_4 \end{aligned}\right\} = \left\{\begin{aligned} &\frac{\Delta^2}{4}(\varepsilon_1 + \varepsilon_2 + \varepsilon_3 + \varepsilon_4)\dot{E}_0 \\ &+ \frac{\Delta^2}{4}(\gamma_1 + \gamma_2 + \gamma_3 + \gamma_4)E_0 \\ &+ \Delta^2 v_0 \rho + O(\Delta^2) \end{aligned}\right.$$

This problem - causing slightly complicated expressions - can be avoided by allocating the permittivities to cells of G and the permeabilities to cells of $\tilde{G}$ instead of allocating both to cells of G, see section 2.3.

There are too more equations that we have not yet looked at and these are the third and fourth Maxwell's equation (3) and (4). Once again we find that the natural choice of the grids G and $\tilde{G}$ and the allocation of the unknown components implicitly satisfy both these equations as has been shown elsewhere[3]. In any volume that consists of cells of G the magnetic flux density is source free "a priori" and similarly the total current is source free in volumes made out of cells of $\tilde{G}$.

This implicit solution of eq. (3) and (4) represents a unique tool for independently testing the numerical results for correct computing and correct coding.

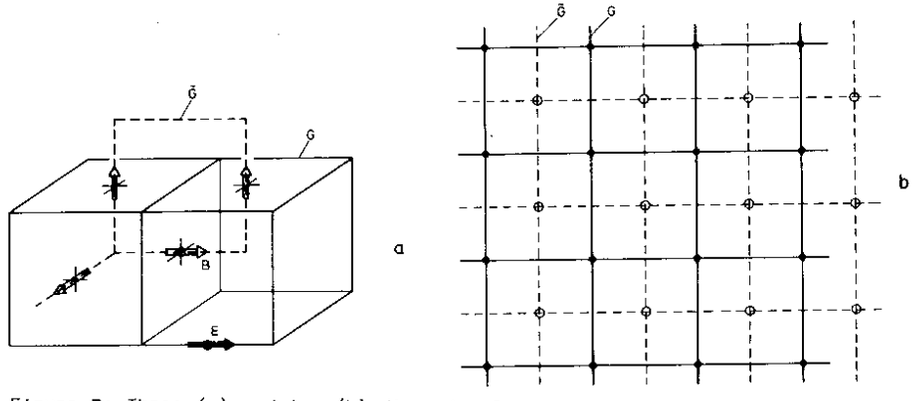

Figure 7: Three (a) and two (b) dimensional examples for dual "electric" and "magnetic" grids G and $\tilde{G}$

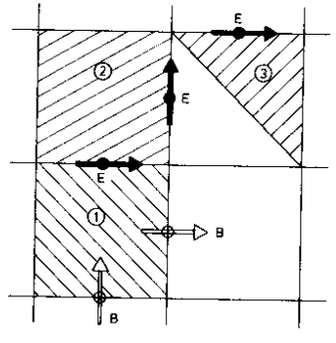

Figure 8: Section of a 2D-mesh with several different materials (1, 2 and 3) demonstrating that only continuous components of $\vec{E}$ and $\vec{B}$ occur

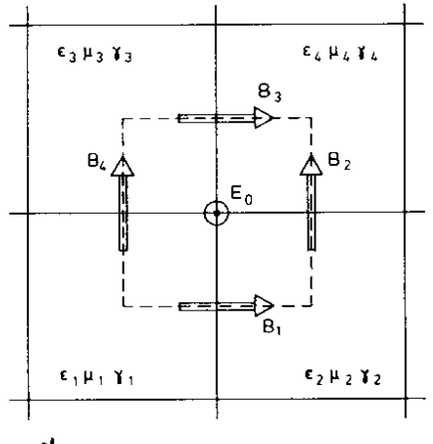

Figure 9: Cell of $\tilde{G}$ for demonstration of the solution of Maxwell's second equation

Now that the basic cell solutions for Maxwell's equation are derived we use any system of numbering all unknowns in a grid. Assembling all the components into vectors yields:

$$\vec{b} = (B_{x_1}, B_{x_2}, \ldots, B_{xN}, B_{y_1}, \ldots B_{zN})^t, \tag{14}$$

$$\vec{e} = (E_{x_1}, E_{x_2}, \ldots, E_{xN}, E_{y_1}, \ldots E_{zN})^t, \tag{15}$$

$$\vec{j} = (J_{dx_1} + \rho \cdot v_{x_1}, \ldots \quad)^t, \tag{16}$$

Maxwell's equation read now in the fully general matrix formulation:

$$R\,\vec{e} = -\dot{b} \quad \Longleftrightarrow \quad \oint \vec{E} \cdot d\vec{s} = -\iint \frac{\partial \vec{B}}{\partial t} \cdot d\vec{A} \tag{17}$$

$$\tilde{R}\,\vec{b} = D_\varepsilon \dot{\vec{e}} + D_\gamma \vec{e} + \vec{j} \quad \Longleftrightarrow \quad \oint \vec{H} \cdot d\vec{s} = \iint \left(\frac{\partial \vec{D}}{\partial t} + \gamma \vec{E} + \rho \cdot \vec{v}\right) d\vec{A} \tag{18}$$

R and $\tilde{R}$ are sparse matrices with four bands and zeros otherwise. D_ε is a diagonal matrix holding the permittivity expressions in (13). Similarly D_γ represents the averaged conductivity as it appears in eq. (13).
Without any specification or specialization we now have found a discrete replacement for Maxwell's equations in their full generality. This discrete form - which is very convenient for use of large scale computers - may now be applied to all those problems that Maxwell's equations apply to.

It is known from e.g. electrostatic problems that one does not need to include all field components in all applications. There are various limits such as the static case or the low frequency limit and we will subdivide Maxwell's equations according to the physical (approximative) limits. The general form of Maxwell's discrete equations consits out of two matrix sets each of which has 3N equations (order r of the matrix is 3N) in a grid of N nodes. Each unknown component is real.
In the frequency domain the two matrix equations can be combined into a single one of order 3N with complex or real elements and unknowns.
In a purely static case only a single unknown (scalar potential) is necessary per node thus yielding a matrix equation of order N.
In parallel with the physical limit we also find that the order of the final matrix equation characterizes the complexity of the physical problem. The following table summarizes the specializations that can be made.

T A B L E I

Specializations for Maxwell's equations in various limits and the corresponding order r of the equivalent discrete Maxwell-matrix equations in a grid of N nodes. The restricted matrix sizes for various applications is explained in the following chapters.

Specification	limit	Type/order r of matrix
magnetostatics electrostatics current flow	$\frac{\partial}{\partial t}(\vec{E}, \vec{H}) \equiv 0$	r = N, real
low frequency	$\frac{\partial}{\partial t}(\vec{E}, \vec{H}) = i\omega(\vec{E}, \vec{H})$ $\lvert\varepsilon\dot{\vec{E}}\rvert \ll \lvert\gamma\vec{E}\rvert$	N < r < 3N, complex or real
high frequency	$\frac{\partial}{\partial t}(\vec{E}, \vec{H}) = i\omega(\vec{E}, \vec{H})$	2N < r < 3N, real or complex
time domain	-------	3N < r < 6N, real

Since static problems need a separate discussion they will be treated in the next section.

2.2 Static problems

In the static case - where all fields are time independent - Maxwell's equations split into decoupled sub sets for electrostatic fields and magnetostatic field (the electrostatic case also includes stationary current flow problems). Since the coupling between electric and magnetic fields is essential in proving that the third and fourth Maxwell's equation are automatically satisfied[3] in the grids G and $\tilde{G}$ by the numerical fields $\vec{e}$ and $\vec{b}$, we can no longer neglect these equations but we will instead have to solve them explicitly.
Let us consider the electrostatic case as an example. Maxwell's equations reduce to:

$$\oint_{(A)} \vec{E} \cdot d\vec{s} = 0 \tag{19}$$

$$\iint_{(V)} \vec{D} \cdot d\vec{A} = \iiint_{V} \rho \, dV \tag{20}$$

In principle we could still use the general matrix form (17) of Maxwell's equations for (19):

$$R \cdot \vec{e} = 0 \tag{21}$$

Since equation (20) has not yet been explicitly solved we have to derive an additional matrix equation replacing (20) of the form:

$$S \cdot D_\varepsilon \vec{e} = \vec{q} \tag{22}$$

Integrating the electric flux density over the surface of a mesh cell of G yields - see figure 10 -:

$$\Delta^2\varepsilon_0 E_2 - \Delta^2\varepsilon_0 E_1 + \Delta^2\varepsilon_0 E_4 - \Delta^2\varepsilon_0 E_3 + \Delta^2\varepsilon_0 E_6 - \Delta^2\varepsilon_0 E_5 = Q_0 \tag{23}$$

If the eight cells of G involved in this integration were filled with different permittivities each ε_0 in the above equation would have to be the average of four different permittivities - see also eq. (13) -. For simplicity we take here vacuum in all cells. Setting up an equation of type (23) for each node yields the matrix equation (22).
In principle the problem is now reduced to the two matrix equations (21) and (23) for the unknown electric field $\vec{e}$ as a function of geometry and charge distribution $\vec{q}$. It is on the other hand well known that this set of equations is largely "overdimensionned" and that static problems can be described by scalar potentials thus reducing the order of the matrices by a factor of three - one single scalar potential instead of three vector components -.

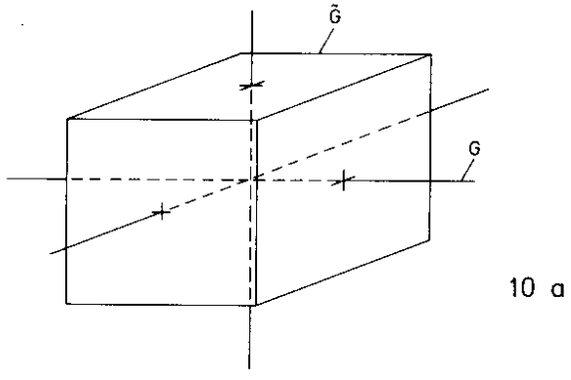

10 a

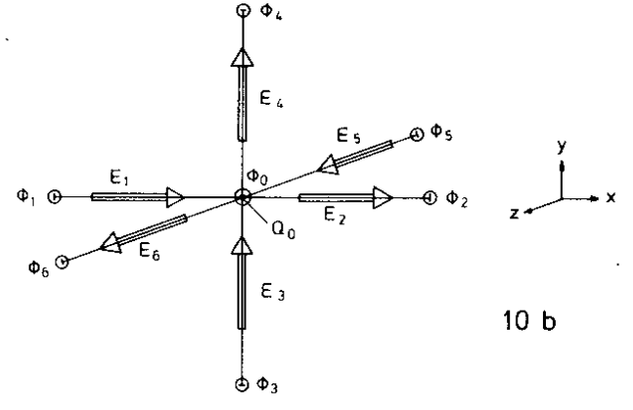

10 b

Figure 10: Mesh cell of $\tilde{G}$ (a) and six electric field components allocated to the six surface areas (b)

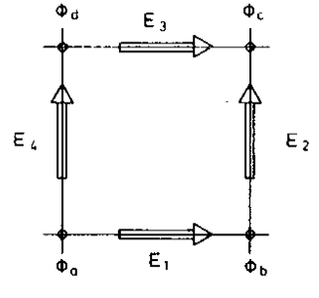

Figure 11: Mesh cell of G with four electric field components associated scalar potentials

With the usual ansatz:

(24) $\vec{E} = -\operatorname{grad} \Phi$

we have to allocate the potential to the grids G and $\tilde{G}$. Once more we find the proper locations through the approximation used for the derivative:

(25) $$\left.\frac{\partial f(x)}{\partial x}\right|_{x=x_0} = \frac{1}{\Delta}\left[f\left(x_0 + \frac{\Delta}{2}\right) - f\left(x_0 - \frac{\Delta}{2}\right)\right] + O(\Delta^2)$$

The left hand side represents a field component whereas the right hand side is the difference of two potentials. Thus Eq. (25) fixes the potentials to the grid nodes of G as shown in figure 10b. Similarly the scalar potential for a magnetic field is consequently fixed to nodes of $\tilde{G}$.
As in the analytic case we readily verify that eq. (19) is a priori satisfied on the mesh too as a consequence of the ansatz (24), see figure 11:

(26) $$\oint \vec{E} \cdot d\vec{s} = \Delta E_1 + \Delta E_2 - \Delta E_3 - \Delta E_4$$
$$= (\Phi_a - \Phi_b) + (\Phi_b - \Phi_c) - (\Phi_d - \Phi_c) - (\Phi_a - \Phi_d) \equiv 0 \ .$$

At this moment it seems worthwhile to remark that it is not trivial that the numerical models are consistent with the analytical equations as is the case here.
The equation remaining is now the "source" equation (22) and (23) respectively. Replacing in (23) each electric field component by the difference of two scalar potentials finally yields - see figure 10 -:

(27) $$6\Phi_0 - \Phi_1 - \Phi_2 - \Phi_3 - \Phi_4 - \Phi_5 - \Phi_6 = \varepsilon_0 \cdot Q_0/\Delta$$

In general the equations have more complicated coefficients caused by different permittivities but for any static problem we find that all equations of type (27) for all N nodes form a matrix equation of the order N with 7 bands (5 in two dimensional cases) and an inhomogeneous vector - representing the charges in electrostatics -:

(28) $$A\vec{\varphi} = \vec{c}$$

This general static matrix equation is only of the order N instead of 3N as in the case where field components are used.

2.3 Extensions and generalisations

When we started to solve Maxwell's equations with a grid the decision to begin with Eq. (1) was somewhat accidental. This starting point immediately generated the mesh G and the approximation of general structures by cells of G so that the only restriction was to have constant material properties in each cell but different ones from cell to cell.
If we had started with the second Maxwell's equation we would have defined the magnetic grid $\tilde{G}$ first and the material properties would have been defined constant in cells of $\tilde{G}$ and not G. Furthermore the unknown quantities would have been interchanged: $\vec{h}$ instead of $\vec{b}$ and the total current $\vec{g}$ instead of $\vec{e}$. The magnetic field in this case would be represented by tangential components and not by perpendicular ones.
We could also have chosen a third way by defining the material properties ε and γ to be constant in cells of the electric mesh G and μ to be constant in a magnetic cell of $\tilde{G}$. In this third case the unknowns would be $\vec{e}$ and $\vec{h}$, see Table II.
Which case of the three listed in Table II is the adequate one will be different from problem to problem: the $\vec{e}$-$\vec{b}$ choice seems adequate for electrostatics whereas the $\vec{g}$-$\vec{h}$ choice is the best for magnetostatics. The $\vec{e}$-$\vec{h}$ set is the best for all coupled electromagnetic problems.

Another set of conditions has not been addressed yet and that is the boundary conditions. In order to obtain unique solutions of Maxwell's equations - and also of the finite matrix equations - we have to satisfy boundary conditions at the outmost surface of a closed volume which need not necessarily be the surface of the grid. The boundary conditions are readily satisfied by setting all those components to zero that lie parallel to the surface of the infinitely conducting or permeable material or to the outmost surface of the grid G. In no case are special sets of equations necessary for boundaries.

Figure 12 shows some possible non cartesian grids in orthogonal coordinate systems to which the FIT method can be applied.

Although the combination of rectangular meshes with triangular sub cells allows good approximations in many cases - see e.g. figure 3 - the question arises of whether a fully irregular mesh made out of triangles would also be compatible with the FIT method. Such fully triangular meshes - as used in the finite element approach - in general allow much better approximations of complicated shapes.

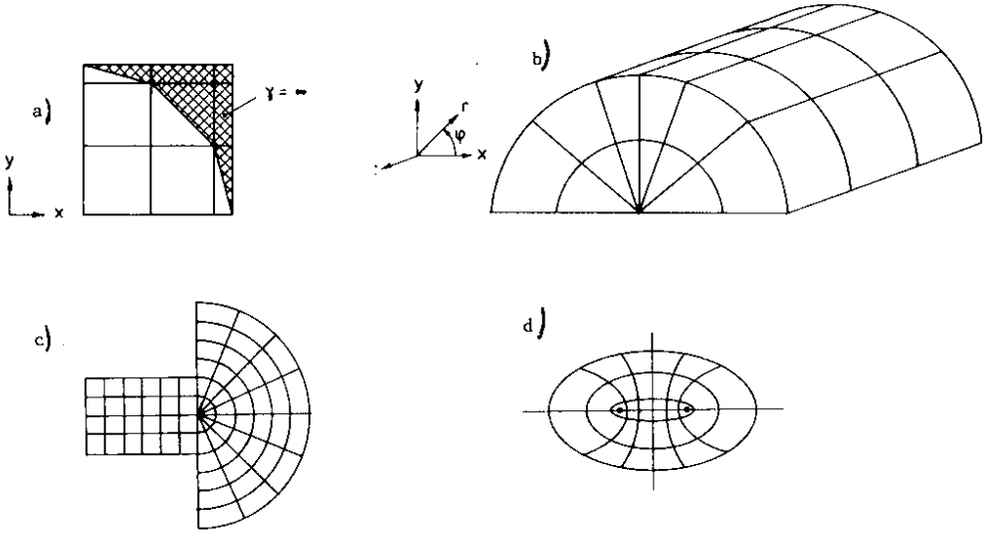

Figure 12: Possible grids for approximating 2D and 3D problems
a) cells are partially filled with infinitely conducting metal in order to allow boundary conditions to be specified along curved lines
b) typical 3D (r, φ, z)-grid adequate for focussing magnets
c) combined cartesian/cylindrical grid for investigating radiation antenna problems
d) elliptical grid for 2D or 3D meshes

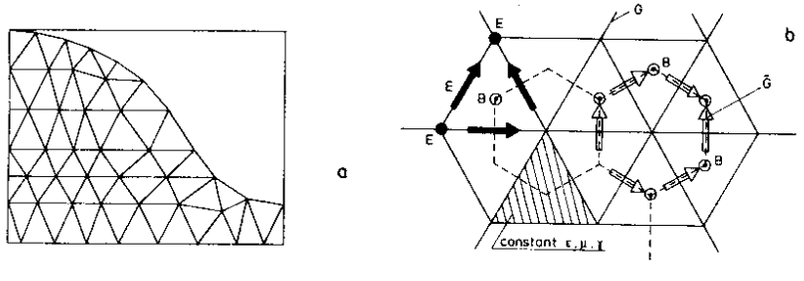

Figure 13: Two dimensional fully triangular grids enabling much better approximation of odd shaped structures (a) and section of a triangular grid showing cells of G with electric field components and dual hexagonal cells of $\tilde{G}$ with magnetic flux density components

constant material properties allocated		unknowns used (defined as continuous)	Maxwell's matrix equations	case
G	$\tilde{G}$			
$\varepsilon\ \gamma\ \mu$	-----	$\vec{e}, \vec{b}$	$R\vec{e} = -\dot{\vec{b}}$ $\tilde{R}\vec{b} = D_\varepsilon\dot{\vec{e}} + D_\gamma\vec{e} + \vec{j}_d$	I
ε, γ	μ	$\vec{e}, \vec{h}$	$R\vec{e} = -D\dot{\vec{h}}$ $\tilde{R}\vec{h} = D_\varepsilon\dot{\vec{e}} + D_\gamma\vec{e} + \vec{j}_d$	II
----	$\varepsilon\ \gamma\ \mu$	$\vec{j}_e, \vec{h}$ $\lvert D_\varepsilon\dot{\vec{e}}\rvert \ll \lvert D_\gamma\vec{e}\rvert$	$RD_\gamma^{-1}\vec{j}_e = -D_\mu\dot{\vec{h}}$ $\tilde{R}\vec{h} = \vec{j}_e + \vec{j}_d$	IIIa
----	$\varepsilon\ \gamma\ \mu$	$\underline{\vec{g}}, \underline{\vec{h}}$ $(\frac{\partial}{\partial t} = i\omega)$	$R(i\omega\underline{D}_\varepsilon + D_\gamma)^{-1}\underline{\vec{g}} = -i\omega\underline{D}_\mu\underline{\vec{h}}$ $\tilde{R}\underline{\vec{h}} = \underline{\vec{g}} + \underline{\vec{j}}_d$	IIIb

Table II: Three possible ways of allocating constant material properties to the electric or magnetic grid G or $\tilde{G}$. Note that the third case is not generally applicable since the total current $\vec{g}$ defined as $\vec{g} = D_\varepsilon\dot{\vec{e}} + D_\gamma\vec{e}$ does not allow recalculation of $\vec{e}$ as necessary for the first Maxwell's equation. In the limit $|D_\varepsilon\dot{\vec{e}}| \ll |D_\gamma\vec{e}|$ (displacement current negligible, $\vec{g} \equiv \vec{j}_e$) the electric field can be obtained from $\vec{e} = D_\gamma^{-1}\vec{g}$ (case IIIa) and for time harmonic fields from $\underline{\vec{e}} = (i\omega\underline{D}_\varepsilon + D_\gamma)^{-1}\vec{g}$ (case IIIb).

The FIT method is also in its full generality applicable to the triangular grids as shown in figure 13. Figure 13b shows the triangular "electric" mesh G made out of triangles and the associated "magnetic" grid $\tilde{G}$ which now consists of hexagonal cells. The dual grid $\tilde{G}$ is constructed in analogy with the rectangular case. One restriction has to be made in order to ensure that the nodes of $\tilde{G}$ always lie inside cells of G - this is necessary when solving the first or second Maxwell's equation - and that is that no angle exceeds 90° in any triangle. This restriction - which is not needed in other numerical methods such as scalar finite elements - is easy to meet as shown in example of figure 13a.

The matrix formalism stays the same in such triangular meshes but in addition book keeping is necessary for the directions of all the unknown elements of $\vec{e}$ and $\vec{b}$ - which were just the directions of the unit vectors in the rectangular approach -.
Similarly one may draw three dimensional non rectangular double grids $G - \tilde{G}$ but the (enormous) price one has to pay for this improved approximation potential is the increased amount of necessary programming and debugging.

3. Applications in the field of accelerator physics

3.1 Magnetostatics, Electrostatics, Stationary Currents
- Bending and focussing magnets, solenoids, separator plates, heat distribution -

In the magnetostatic limit Maxwell's equations reduce to:

$$(29) \qquad \oint_{(A)} \vec{H} \cdot d\vec{s} = \iint_{A} \vec{J}_d \cdot d\vec{A}$$

$$(30) \qquad \iint_{(V)} \mu\vec{H} \cdot d\vec{A} = 0$$

$\vec{J}_d$ represents a given distribution of driving currents and the permeability is in general a tensor - see e.g. laminated transformer cores - the elements of which are nonlinear functions of the magnetic field strength:

$$(31) \qquad \mu = (|\vec{H}|)$$

From eq. (29) it follows that the magnetic field $\vec{H}$ cannot be represented by the gradient of a scalar potential since $\vec{H}$ is not "curl free".
In order to maintain the simplicity of static problems and scalar potentials it is useful to split the total magnetic field $\vec{H}$ into a source field $\vec{H}_s$ plus a gradient of a scalar potential:

$$(32) \qquad \vec{H} = \vec{H}_s - \operatorname{grad} \Phi$$

With this ansatz we obtain instead of (29) and (30):

$$(33) \qquad \oint_{(A)} \vec{H}_s \cdot d\vec{s} = \iint_{(A)} \vec{J}_d \cdot d\vec{A}$$

$$(34) \qquad \iint_{(V)} \mu \operatorname{grad} \Phi \cdot d\vec{A} = \iint_{(V)} \mu\vec{H}_s \cdot d\vec{A}$$

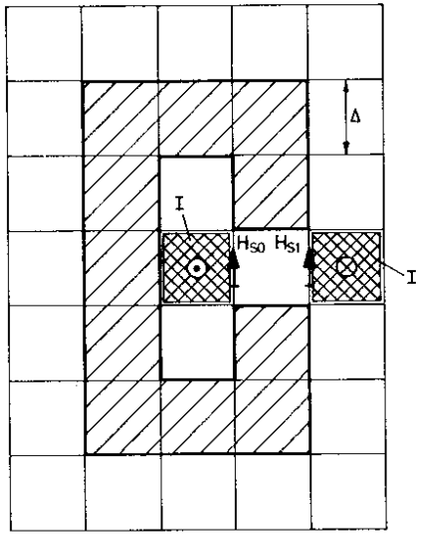

Figure 14: Schematic cross section of a C-shaped bending magnet with return current and the only two components of the source field $\vec{H}_s$ in the grid that need to be nonzero

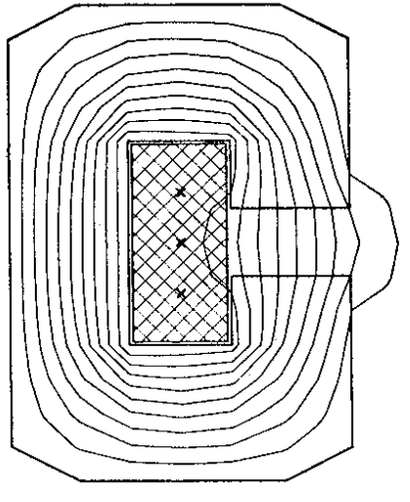

Figure 15: Magnetic flux density in a C-shaped magnet

Eq. (33) can now be solved separately before (34) for example by the Bio Savart law:

$$(35) \qquad \vec{H}_s(\vec{r}_o) = \frac{1}{4\pi} \iiint_V \vec{J}_d \times \operatorname{grad} \left(\frac{1}{|\vec{r} - \vec{r}_o|} \right) d^3r$$

Once $\vec{H}_s$ is known the right hand side of Eq. (34) is given and the final equation to be solved is reduced to one for the scalar potential Φ.

This method of scalar potentials for static problems was developed since more than fifteen years ago and successfully applied to many technical problems in two ane three dimensions[4-8]. Although the splitting of the magnetic field into a "curly" source part and a scalar potential part finally reduces the problem to a purely scalar one there is still a significant amount of effort (i.e. cpu time) necessary to evaluate the Bio Savart integral for all grid nodes since $\vec{H}_s$ must be known everywhere.

Furthermore it has been found that in iron regions $\vec{H}_s$ and grad φ tend to become similar in magnitude yielding cancellation errors[9] for the final field $\vec{H}$, see Eq. 32 . Both disadvantageous facts, the cpu time and the cancellation do not apply to another procedure for solving Eq. (33) that makes use of the fact that $\vec{H}_s$ need not be a physical meaningful field but is just an intermediate vector field used to reduce the size of the problem[10]. This method can be simply demonstrated by figure 14. Only two non zero components of the source field in the whole mesh are needed in order to satisfy Eq. (33):

$$(36) \qquad H_{so} = I/\Delta \,, \quad H_{s1} = H_{so} = I/\Delta$$

Although this $\vec{H}_s$ is very unphysical it does the necessary job of removing the "curly" part from the total field. The gradient of the scalar potential will subsequently be used to ensure that the total field is source free. Even in large 3D meshes this surprisingly simple method for constructing a source field only negligile cpu time whereas the Bio Savart algorithm uses a significant fraction of the total cpu time for solving a problem.

Furthermore in many cases, this procedure finds - as in the one shown in fig. 14 - solutions with no $\vec{H}_s$ in the metal and with only a few non zero source field components thus avoiding cancellation problems.

Once the source field is known and equation (34) has been solved for all nodes we obtain a matrix equation for all unknown potentials (assembled in $\vec{\varphi}$) for a given $\vec{H}_s$ (represented by $\vec{c}$) - see section 2.2 -:

$$(37) \qquad A\vec{\varphi} = \vec{c}$$

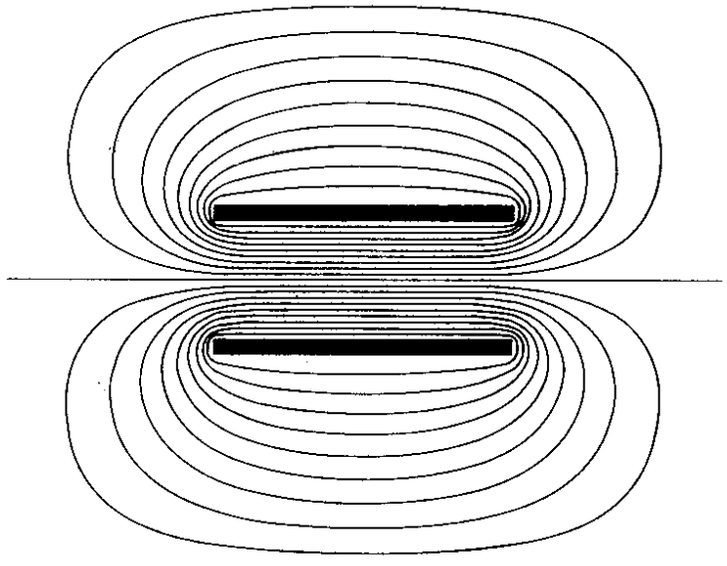

Figure 16: Equipotential lines of a parallel plate capacitor (electrostatic deflector)

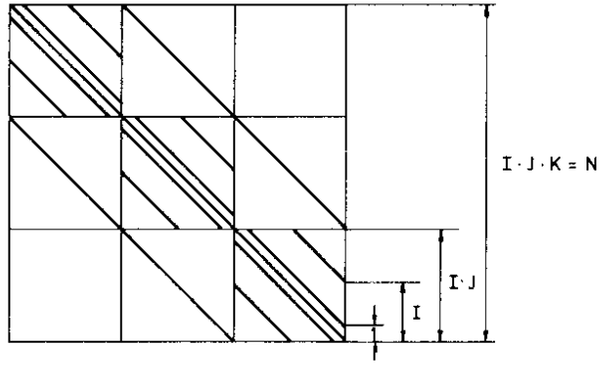

Figure 17: Structure of a 3D static matrix. The bands indicate nonzero elements. I, J and K are the numbers of grid lines in the three spatial directions. The number of rows between the elements is indicated on the right

Since the permeability tensor elements are field dependent A and $\vec{c}$ depend on the total field strength too - which is yet not known -. The obvious - and usual - way of solving this non-linear saturation problem is to start with a uniform distribution of μ and to compute the fields. Then the μ's in each cell are updated according to the calculated field strength. This procedure is repeated until convergence appears. "Inside" each step the seven banded matrix equation (37) has to be solved with one of the commonly used iterative methods[11]. Figure 15 shows a simple example computed with the program PROFI[12].

In the electrostatic case the corresponding two field equations read:

$$\oint_{(A)} \vec{E} \cdot d\vec{s} = 0 \tag{38}$$

$$\iint_{(V)} \varepsilon \vec{E} \cdot d\vec{A} = \iiint_{V} \rho \cdot dV \tag{39}$$

Here no source field is needed and the driving term is directly given on the right hand side of (39). The derivation of the - now mostly linear - equations yield a matrix equation almost identical to (37). A simple example of an electrostatic application of PROFI[12] is shown in figure 16. If we leave for a moment the integral notation of the field equations we find that the general static potential differential equation reads:

$$\operatorname{div}[\alpha(\vec{r}) \operatorname{grad} X(\vec{r})] = S(\vec{r}) \tag{40}$$

The meaning of α, X and S is shown in Table III. It is clear from this consideration that a general computer code solves for electrostatics, magnetostatics, stationary currents and stationary heat flow problems as well.

Table III: The general potential equation for electric or magnetic potentials (Φ^E, Φ^H) or temperatures (T)

$\operatorname{div}[\alpha(\vec{r}) \operatorname{grad} X(\vec{r})] = S(\vec{r})$				
case	α	X	S	result
electrostatics	ε	Φ^E	ρ	$\vec{E} = -\operatorname{grad}\Phi^E$
magnetostatics	μ	Φ^H	$\operatorname{div}\mu\vec{H}_s$	$\vec{H} = \vec{H}_s - \operatorname{grad}\Phi^H$
stationary currents	γ	Φ^E	$\operatorname{div}\vec{J}_d$	$\vec{J} = -\gamma\operatorname{grad}\Phi^E$
temperature	λ	T	W	T

More sophisticated applications to heat problems and induction motors may be found in the literature[12, 13].

Finally it should be briefly demonstrated how the matrices are structured since the structure is very important when matrices become very large (over 1000 x 1000). The general 3D matrix is blocked and seven banded. Each block belongs to one plane of the grid. With a linear numbering system and I, J and K grid lines in the three directions we obtain a matrix structure as shown in figure 17. The matrix is real and symmetric. The order rarely exceeds 100.000 x 100.000. The 2D case matrix is identical to a single diagonal block with five bands.

Programs concurrent to PROFI[12] - that are widely used - are the Rutherford developments GFUN[14] and TOSCA[15] both based on rather different approaches.

3.2 Low frequency eddy currents
- eddy currents in synchrotron magnets -

Eddy current problems usually occur in the domain of relatively low frequencies, e.g. power frequencies. This regime is governed by the fact that the wave length of the driving currents - we assume harmonic fields here - is large compared to the dimensions of the apparatus to the investigated. In these cases the displacement current is small compared to the eddy current:

$$|i\omega\varepsilon\underline{\vec{E}}| \ll |\gamma\underline{\vec{E}}| \tag{41}$$

$$\vec{E}(\vec{r}, t) = \operatorname{Re}\{\underline{\vec{E}}(\vec{r})\, e^{i\omega t}\} \tag{42}$$

The driving term in Maxwell's equations is given by prescribed driving currents ($\underline{\vec{J}}_d$) in addition to the eddy currents ($\underline{\vec{J}}_e = \gamma\underline{\vec{E}}$). With these definitions and the assumption (41) Maxwell's equations in the low frequency limit read:

$$\oint_{(A)} \underline{\vec{E}} \cdot d\vec{s} = -i\omega \iint_{A} \mu\underline{\vec{H}} \cdot d\vec{A} \tag{43}$$

$$\oint_{(A)} \underline{\vec{H}} \cdot d\vec{s} = \iint_{A} (\gamma\underline{\vec{E}} + \underline{\vec{J}}_d) \cdot d\vec{A} \tag{44}$$

At this point the question arises of why one treats low frequency problems separately from the general case for which matrix equations have been derived earlier, see (17) and (18) and Table III. The answer is that in air - where γ vanishes - the electric and the magnetic field are not fully coupled - we explicitly neglected the coupling term $i\omega\varepsilon\underline{\vec{E}}$ -. This in turn enables a quasi static ansatz in air. As a consequence we will end up with a matrix which does not have the full size of 3N as in the general case.

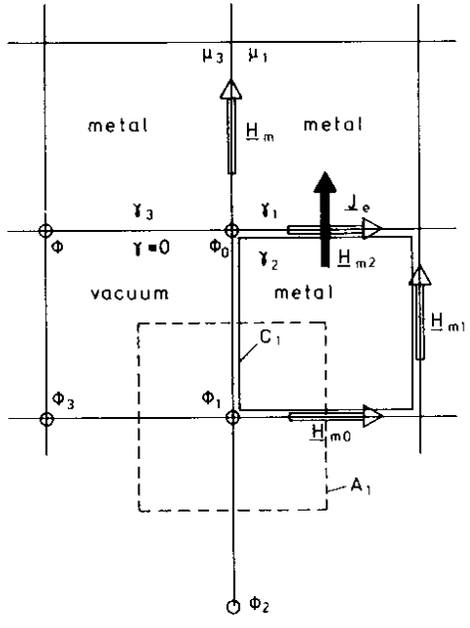

Figure 18: Section of mesh $\tilde{G}$ used for low frequency eddy current problems. Material properties are constant in cells of $\tilde{G}$ and continuous unknowns are the magnetic (tangential) field plus the (perpendicular) current density. Scalar potentials are defined in non conducting regions and on the surface of conducting volumes

It is a general rule that one should reduce the order of the matrix as far as possible in order to avoid numerical problems - as we did in the static case where only N equations instead of 3N were finally used -.
Independently of whether γ vanishes or not we can "a priori" split the magnetic field into a source part and a non-source part. We choose to start with a magnetic mesh $\tilde{G}$ (case IIIa of table II) and define material properties to be constant in cells of $\tilde{G}$. Consequently, the unknowns are the magnetic field and the current density, see fig. 18. The source part of the magnetic fields obeys:

$$(45) \qquad \oint_{(A)} \vec{\underline{H}}_s \cdot d\vec{s} = \iint_A \vec{\underline{J}}_d \cdot d\vec{A} \ ,$$

and can be computed as described for static fields in section 2.2. We consider $\vec{\underline{H}}_s$ to be given from now on and distinguish further between conducting areas and non-conducting areas. The total vacuum field $\vec{\underline{H}}_v$ obeying:

$$(46) \qquad \oint_{(A)} \vec{\underline{H}}_v \cdot d\vec{s} = \iint_A \vec{\underline{J}}_d \cdot d\vec{A} \ ,$$

$$(47) \qquad \oint_{(A)} \vec{\underline{E}} \cdot ds = - i\omega \iint_A \mu_o \vec{\underline{H}}_v \cdot d\vec{A} \ ,$$

$$(48) \qquad \iint_{(V)} \mu_o \vec{\underline{H}}_v \cdot d\vec{A} = 0 \ ,$$

can be split into the previously defined source field plus a scalar potential gradient:

$$(49) \qquad \vec{\underline{H}}_v = \vec{\underline{H}}_s - \text{grad } \underline{\Phi}$$

The electric field has no feed back to the magnetic field and we may neglect eq. (47) for the moment. From (48) and (49) we find that the scalar potential is essentially the same as in the purely static case the only difference being that it now may have complex values. Thus the matrix for such vacuum or non-conducting node equations is similar to the static one: - see eq. (27) and (28) -. Note that the order of A is now only N_V (N_V = number of vacuum nodes, $N_V < N$).

$$(50) \qquad A_V \underline{\varphi} = \vec{\underline{c}}_V$$

Once the potential is known and thus the magnetic field, the electric field may be subsequently calculated from eq. (47).

a)

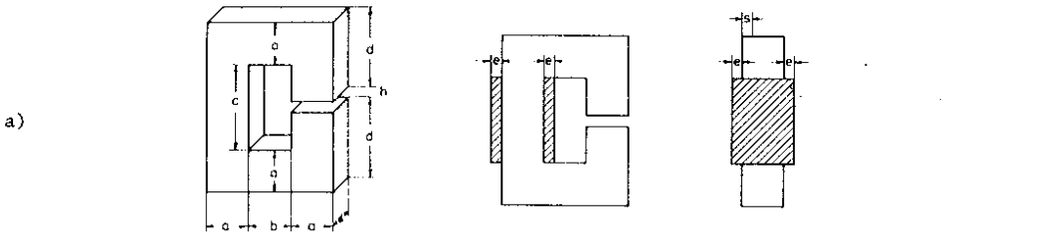

b)

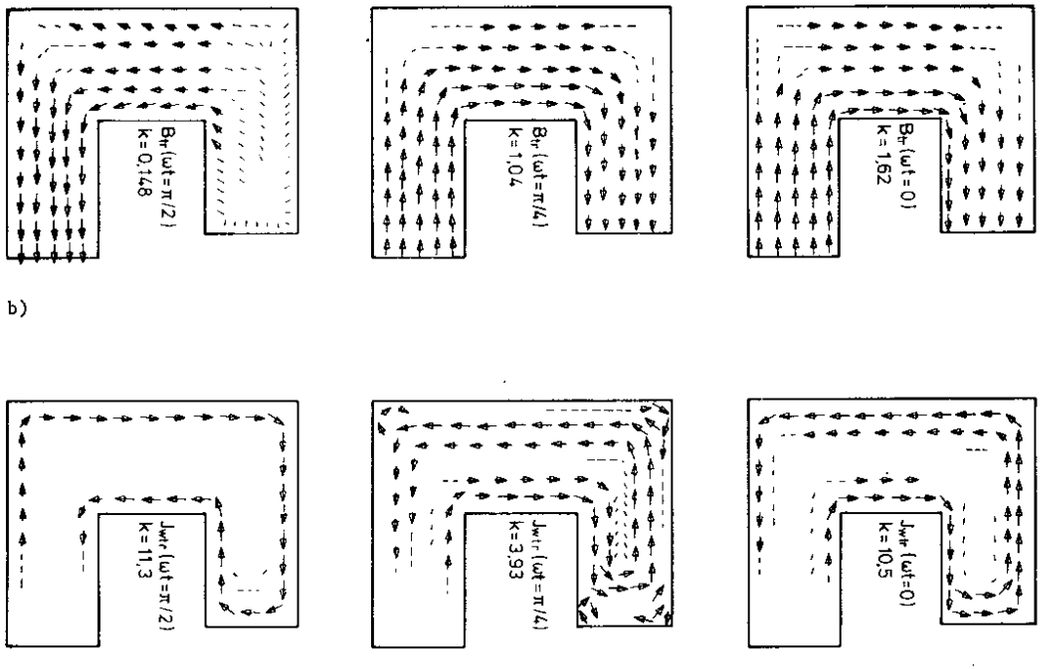

Figure 19: a) Three dimensional laminated magnet circuit with air gap and 50 Hz excitation coils
a = 8 cm; b = 8 cm; c = 16 cm; d = 15 cm; e = 2 cm; h = 2 cm; f = 50 Hz; Lamination filling factor 0.98; $\mu = 2000\mu_0$; conductivity $\gamma = 0{,}85\ 10^6\ Sm^{-1}$
b) Eddy currents and magnetic flux in a metal sheet at s = 3.5 cm from the surface at three time points. k gives the relative strength of the longest arrows

In conducting regions Maxwell's equations are fully coupled. Assuming solid metal - otherwise D_γ^{-1} is not defined - we use the full matrices (see Table II, case IIIa):

$$R\, D_\gamma^{-1}\, \vec{j}_e = -i\omega\, D_\mu\, (\vec{h}_m + \vec{h}_s), \tag{51}$$

$$\tilde{R}\, \vec{h}_m = \vec{j}_e \tag{52}$$

Here we split the magnetic field into the precalculated source part $\vec{H}_s$ and a "metal" part $\vec{H}_m$. The driving current does not appear in eq. (52) since the precalculated source field is solution of

$$\tilde{R}\, \vec{h}_s = \vec{j}_d \tag{53}$$

Rearranging the two matrix equations (51) and (52) finally yields:

$$[R\, D_\gamma^{-1}\, \tilde{R} + i\omega\, D_\mu]\, \vec{h}_m = -i\omega\, D_\mu\, \vec{h}_s \tag{54}$$

For short we write instead of (54):

$$A_m\, \vec{h}_m = \vec{c}_m \tag{55}$$

Note that this system of equations is complex.
The two regions - conducting metal and vacuum - are connected by their interfaces at which the tangential field as well as the normal flux density must be continuous. The continuity conditions - that are a major cause of problems for many other approaches - are readily verified by the FIT method: When setting up line integrals for the magnetic field in the conducting region - see curve C_1 in figure 18 - we may simply replace a nonexistent $\vec{H}_m$ component by the gradient of two scalar potentials (Φ_1, Φ_0). When integrating around a node where a potential is defined as unknown - see area A_1 in figure 18 - we simply replace the "missing" gradient by $\vec{H}_{m0}$ in order to satisfy div $\vec{B} = 0$. Summarizing we find that a rather natural way of connecting the two regions is given by setting $\vec{H}_m$ to zero at the interface and Φ to zero (or better "not present") inside the metal. There are furthermore no special matrix coefficients necessary and the setting up of the interface conditions is very easy to program. The final matrix including the coupling is given by:

$$\begin{pmatrix} A_v & C_{vm} \\ C_{mv} & A_m \end{pmatrix} \cdot \begin{pmatrix} \vec{\Phi} \\ \vec{h}_m \end{pmatrix} = \begin{pmatrix} \vec{c}_v \\ \vec{c}_m \end{pmatrix} \quad \begin{matrix} N_v = N - N_m \\ 3\, N_m \end{matrix} \tag{56}$$

With N_m as the number of metal nodes and $N_V \approx N - N_m$ the overall order of the above matrix becomes $r = N + 2\,N_m$. This matrix has complex elements and only the sub matrices A_V and $\underline{A}_m$ show some symmetry properties.
More details of this solid eddy current approach are described in ref. 16 and laminated iron core eddy current problems were solved similarly before[17,18]. The solid case has been coded in a computer code named WIMEK[16,20] for the fully three dimensional case and quasi-three dimensional work is described in ref. 19.
There are other approaches to two and three dimensional low frequency eddy current problems that should be mentioned here. First of all there is the "obvious" choice of vector potentials[21,22] that yields gauging problems and rather complicated interface conditions especially in arbitrarily shaped 3D geometries. Then there is the combined vector/scalar potential approach[23-26] with discontinuity problems of physically continuous quantities at the metal-air interface. Finally there is a modified version of the combined vector/scalar approach with all vector components vanishing at the interface[27,28] (this ansatz is more or less identical with the FIT method described here[16,17]). All these different approaches are - except the one we used here - discussed in more detail elsewhere[28].
Once more we found here that the FIT ansatz - implicitly hidden in Maxwell's equations - directly gave a natural way of attacking the problem. No discontinuity problems or interface complications occur as it is the case when using artificial intermediate functions such as vector potentials.

A relatively important case is not covered so far and that is the problem of eddy currents in laminated iron cores. Let us assume that the lamination plane is perpendicular to the z-direction. In the low frequency limit - where displacement currents are neglected - there is no current in z-direction and the conductivity tensor is given by:

$$\gamma = \begin{pmatrix} \gamma_x & 0 & 0 \\ 0 & \gamma_y & 0 \\ 0 & 0 & 0 \end{pmatrix} \tag{57}$$

This in turn causes D_γ^{-1} to be undefined since D_γ has tensor components on the diagonal and is zero otherwise. Whatever ansatz of table II we use, when reducing the matrix equation to one for the magnetic field $\vec{\underline{h}}$ we always hit Q_γ^{-1}. If we used $\vec{\underline{e}}$ instead of $\vec{\underline{h}}$ we would also run into numerical problems with largely oversized matrices since $\vec{\underline{E}}$ is nonzero in the vacuum too.

Once more the solution is simply arrived at by considering the physics: Since γ_z and $\underline{J}_z$ are zero, the magnetic field in any plane perpendicular to z is "curl free". Thus the field may be described by a "plane" scalar potential. In these planes we do not need two vector components. The only magnetic field component in metal that cannot be taken into account this way in $\underline{H}_z$.
Since scalar potentials are now used in each grid plane we simply use one and the same scalar potential throughout the total grid - in vacuum and iron -. We add to each node inside a conducting region one $\underline{H}_z$ component as unknown in order to account for the eddy currents. This approach is very simple to program since it can be considered to be an extension of the purely static case. More details of the theory may be found elsewhere[17]. The final matrix equation has the form:

$$\begin{pmatrix} A_V & C_{vm} \\ \underline{C}_{mv} & \underline{A}_m \end{pmatrix} \cdot \begin{pmatrix} \vec{\underline{\varphi}} \\ \vec{\underline{h}}_{zm} \end{pmatrix} = \begin{pmatrix} \underline{c}_v \\ 0 \end{pmatrix}; \quad \begin{matrix} N \\ N_m \end{matrix} \tag{58}$$

The order of the matrix is now $N + N_m$ (instead of $N + 2N_m$ for solid metal) and A_V is the normal scalar potential matrix for the total region.
A computer code WILEK [18] has been written that solves for arbitrarily shaped three dimensional lamination problems. A typical result of WILEK is given in figure 19 where the eddy current distribution has been calculated in a fully 3D laminated magnetic circuit.
There is an intermediate region between solid and laminated iron where the geometry has a symmetry which restricts the eddy currents to have only one or two components although the actual object is three dimensional. It is obvious how this kind of problem can be solved with the ansatz used for the lamination and detailed studies have been undertaken for these cases[19]. As one result we show here the eddy current distribution in an air coil in figure 20. Parts of these eddy current programs[16,19,20] have meanwhile been implemented into PROFI[12].

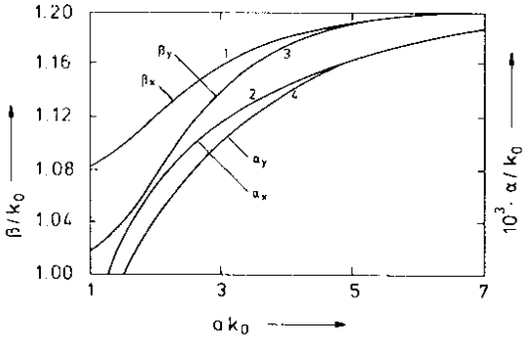

a

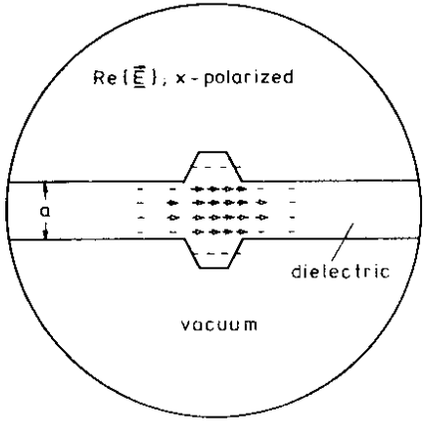

b

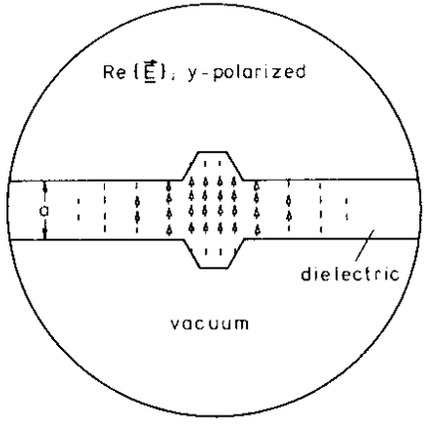

c

Figure 24: Complex propagation constants ($\underline{k}(\omega) = \beta(\omega) - i\alpha(\omega)$) and transverse electric field of the two fundamental waves on a dielectric single material fiber waveguide. All frequencies are normalized to the support thickness a. The fiber material is defined by $\underline{\varepsilon} = 1{,}5\ \varepsilon_0(1 - i\ 0.01)$, $\mu = \mu_0$, $\gamma = 0$ and the circular waveguide is assumed to be infinitely conducting

a) propagation constants for the x and y polarized waves at $ak_0 = 7$
b) electric field of the x polarized wave
c) electric field of the y polarized wave

3.3 High frequency domain

- accelerating rf-cavities, rf-seperators, data transmission lines -

At high frequencies there is no term in Maxwell's equation that one can neglect and we obtain the Maxwell's matrix equations from the general form (17) and (18) - or from table II - by replacing the vectors by their complex phasors:

$$(59) \qquad R\,\vec{\underline{e}} = -i\omega\,\vec{\underline{b}}$$

$$(60) \qquad \tilde{R}\,\vec{\underline{b}} = i\omega\,\underline{D}_\varepsilon\,\vec{\underline{e}} + D_\gamma\,\vec{\underline{e}} + \vec{\underline{j}}$$

We can easily eleminate one of these two equations and obtain:

$$(61) \qquad [R\,(i\omega\,\underline{D}_\varepsilon + D_\gamma)^{-1}\tilde{R} + i\omega\,I]\,\vec{\underline{b}} = [R\,(i\omega\,\underline{D}_\varepsilon + D_\gamma)^{-1}]\,\vec{\underline{j}}_d$$

$$(62) \qquad [\tilde{R}\,R - \omega^2\,\underline{D}_\varepsilon + i\omega\,D_\gamma]\,\vec{\underline{e}} = -i\omega\,\vec{\underline{j}}_d$$

We could have also chosen any other set of table II to obtain similar equations but the easiest and most evident form with respect to ω is eq. (62) with which we will continue here.

We first distinguish between driven problems ($\vec{\underline{j}}_d \neq 0$, $\omega = \omega_0$) and eigenvalue problems ($\vec{\underline{j}}_d \equiv 0$, ω = unknown). From equation (62) we could in principle obtain the electric field for any given $\vec{\underline{j}}_d$ driving term but it turns out that this large and fully complex system of linear equations is hard to solve. Even if we used loss free material (ε real, $\gamma = 0$) it is clear that (62) will be difficult to solve for frequencies near to eigenfrequencies. Physically this is the problem of driving a loss free resonator at resonance. Mathematically the difficulty is hidden in the fact that the diagonal elements decrease below the limit of being diagonally dominant. Most of the iterative methods do not work in this case. A better way of solving such problems is the time domain approach described in the next section.

Probably more important in high frequency technology are the eigensolutions of Maxwell's equations, e.g. resonant frequencies of resonators and dispersion relations for waveguide structures.

The general form of the eigenvalue equation reads:

$$(63) \qquad [\tilde{R}\,R]\,\vec{\underline{e}} = \omega^2\,\underline{D}_\varepsilon\,\vec{\underline{e}} - i\omega\,D_\gamma\,\vec{\underline{e}}$$

This nonlinear eigenvalue problem is not easy to solve not least owing to its complex form. Since for most of the technical applications the loss term due to the non-zero conductivity may be obtained by perturbation theory we neglect for a while D_γ and obtain:

$$(64) \qquad \underline{D}_\varepsilon^{-1/2}\,\tilde{R}\,R\,\underline{D}_\varepsilon^{-1/2}\,\vec{\underline{e}}' = \omega^2\,\vec{\underline{e}}', \qquad \vec{\underline{e}}' = \underline{D}_\varepsilon^{1/2}\,\vec{\underline{e}}$$

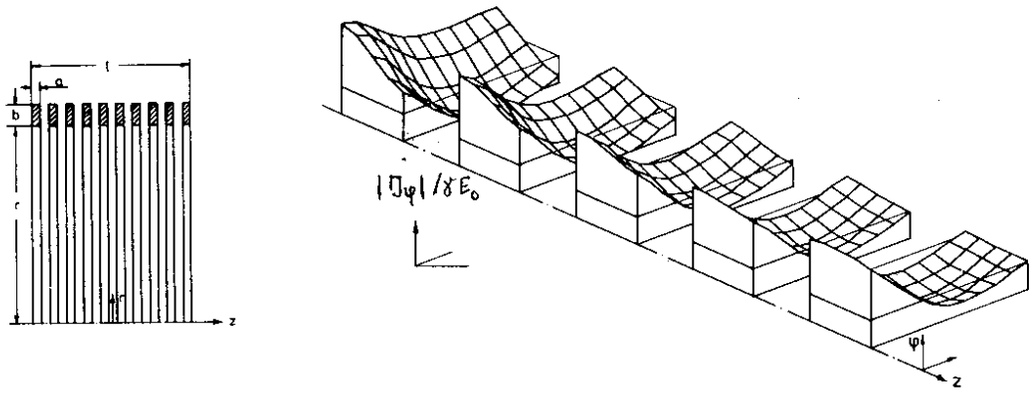

Figure 20: Azimuthal eddy current distribution in a cylindrical air coil (from ref. 19) (a = 2 cm, b = 5 cm, ℓ = 40 cm, r = 50 cm, $\gamma = 5.8\ 10^7 Sm^{-1}$, f = 50 H_z). (Only the left half is shown)
E_0 is the driving electric field.

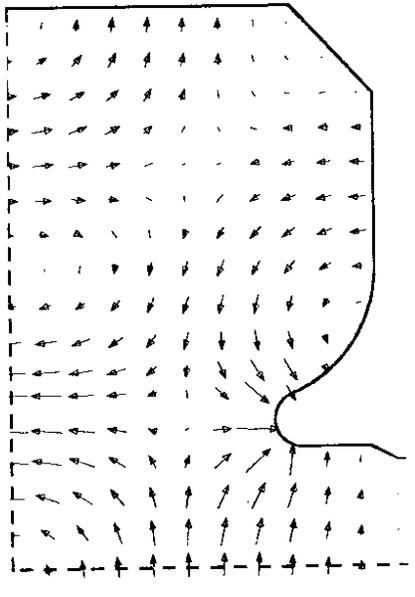

Figure 21: Electric field of the 6-th deflecting parasitic dipole mode in the seven cell PETRA cavity at f = 1905 MHz. Only half a cell of the axially symmetric cavity is shown here.

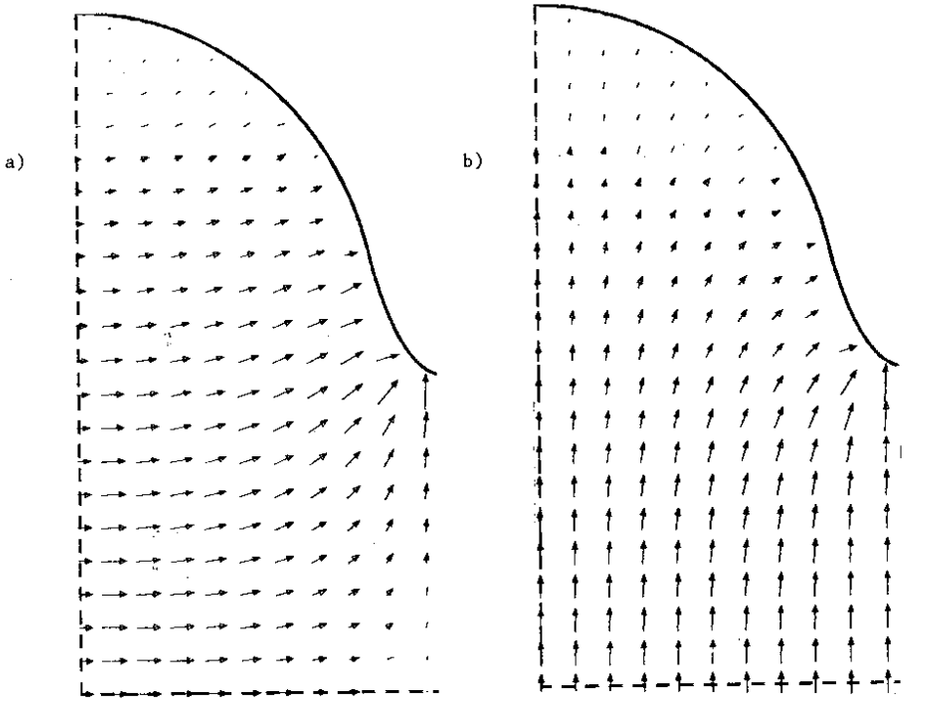

Figure 22: Superconducting "Single Mode Cavity" (SMC) with only one single monople and dipole resonant mode
a) electric field of accelerating fundamental monopole mode
b) electric field of the TE-like dipole mode

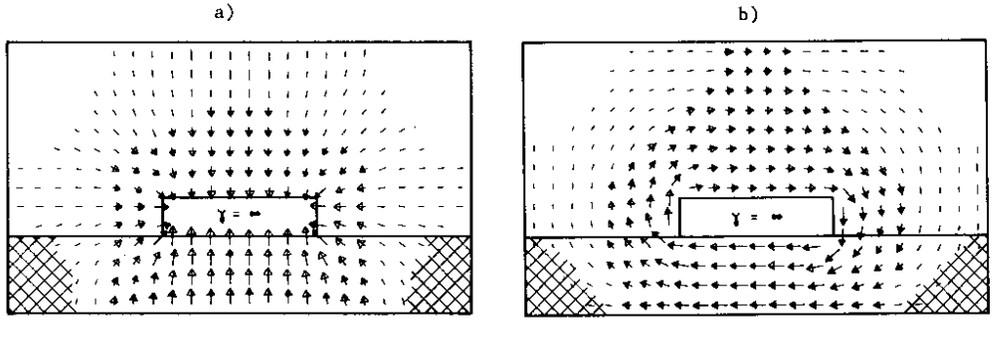

Figure 23: Electric (a) and magnetic (b) field of the fundamental propagating wave on a micro strip transmission line on dielectric support surrounded by a rectangular waveguide (infinitely conducting). Permittivity of the dielectric is $\varepsilon = 1.5\ \varepsilon_0$ and the normalized frequency is $ak_0 = 0.16$ where a is the support thickness

For lossy dielectrics (64) is still a complex eigenvalue problem. In the loss free case we obtain from (64):

$$(65) \qquad [D_\varepsilon^{-1/2}\, \tilde{R}\, R\, D_\varepsilon^{-1/2}]\, \vec{e}' = \omega^2\, \vec{e}', \qquad \vec{e}' = D_\varepsilon^{-1/2}\, \vec{e}$$

Eq. (65) is now a real symmetric simple eigenvalue problem with ω^2 as algebraic eigenvalue. This result is consistent with the physics which allows only real frequencies in loss free resonators.

Fortunately such fully three dimensional resonator problems do not occur frequently in accelerator technology. For accurate calculations such 3D codes need an enormous amount of computing time. A general 3D code for the FIT approach is presently being worked on. Other approaches to the resonator problem are discussed in more detail elsewhere[29].

In many practical cases resonators have some symmetry properties enabling a two dimensional ("2.5" dimensional) treatment of a 3D structure. One of the probably most prominent representatives of this group are the cylindrically symmetric accelerating cavities.

For all these quasi 3D calculations the general 3D matrix in (65) is reduced by roughly 1/3 in its order having only two out of three field components as unknowns:

$$(66) \qquad A \cdot \begin{pmatrix} \vec{x} \\ \vec{y} \end{pmatrix} = \omega^2 \begin{pmatrix} \vec{x} \\ \vec{y} \end{pmatrix} \begin{matrix} N \\ N \end{matrix} \; ;$$

$\vec{x}$, $\vec{y}$ two out of six sets of all unknown field components.

Note that one does not have to choose necessarily $\vec{x}$ and $\vec{y}$ to be both electric or both magnetic field components. For the axis-symmetric cavity case many authors used E_φ and H_φ - see references and discussion in ref. 29 - but the FIT ansatz implicitly uses electric components only or magnetic ones only.

In the case of a symmetry one of the three field components can be eliminated making use of the fact - see section 2.2, eq. (22) - that the third (fourth) Maxwell's equation is implicitly satisfied. In the cavity code URMEL[29,30] the choice was E_r and E_z as unknown and we note that these are the components lying in the grid plane - the grid is only 2D -. As example we show in figure 21 the electric field of a deflecting parasitic dipole mode in the accelerating PETRA[31] cavity[32] (7 cell type) calculated with URMEL.

Investigating and optimizing accelerating cavity modes is an important subject in any accelerator design. On one hand the cavity should be optimized for shunt impedance and on the other hand higher resonant modes may cause severe performance limitations due to instabilities of the particle beams.

In order to avoid multi-turn/multi bunch instabilities caused by higher resonant modes a code such as URMEL is a very useful tool for optimizing the accelerating properties and reducing the parasitic effects at the same time. Figure 22 shows a "Single Mode Cavity"[33] (SMC) that has only one single monopole mode (the accelerating one) and only two less harmful dipole modes. This kind of cavity does not need higher order mode couplers except one for the two deflecting modes. Such cavities - especially when superconducting - may help to remove multi-bunch/multi-turn effects by removing all sharp resonances. In the following sections we will show how such cavities can be optimized for a broader range of requirements by combining FIT-programs in time and frequency domain.

There is a similar area of problems which occur for any structure of constant cross section. If the structure has a finite length it can be considered a cavity, if it is infinitely long we have the general waveguide problem.

By choosing again unknows in the grid plane the FIT method yields directly a complex but linear eigenvalue problem the algebraic eigenvalue of which is the square of the complex propagation constant:

$$(67) \qquad \underline{A}\, \underline{\vec{e}}_\perp = \underline{k}^2\, \underline{\vec{e}}_\perp$$

where $\underline{\vec{e}}_\perp$ denotes the unknown electric field components perpendicular to the wave propagation direction. Note that this system is linear both for lossy dielectric and for conducting materials since $\underline{k}$ is computed for a given ω. A computer code LW[34,35,36,37] has been developed for arbitrarily shaped waveguides made out of tensorial lossy material. Figures 23 and 24 show typical results from LW in the form of the complex propagation constant as a function of frequency for different wave types and their field patterns.

By adding metallic end plates at two z-positions one readily obtains "constant cross section cavities" and from LW the resonant frequencies and damping rates.

3.4 Time domain

- self forces inside charged particle beams -

Magnet design and optimization of accelerating cavities in accelerator physics are probably the best known "applications" of Maxwell's equations and computer codes for solving them. Probably the most important regime to develop during the last decade has been that of the single beam instabilities due to self excited electromagnetic fields. Front line accelerators such as PETRA[31], PEP[38] and the future SLC[40] and LEP[41] and HERA[39] do (will) suffer significantly from such collective effects.

Whenever a bunch of charged particles passes any accelerating structure - such as bellows, accelerating cavities, position monitors etc. - electromagnetic fields are generated that act back on the particles inside the bunch. Since such "wake fields" are excited both by non-resonant structures and resonant structures and since their interaction radius is limited to the bunch length the best way to attack the problem is to use time domain and not the frequency domain[42, 45].

We recall the Maxwell's matrix equation now in its most general time dependent form with $\vec{j}_d$ now given by the current density of moving particles:

$$R\,\vec{e} = -\dot{\vec{b}} \tag{68}$$

$$\tilde{R}\,\vec{b} = D_\varepsilon\,\dot{\vec{e}} + D_\gamma\,\vec{e} + \vec{j}_d \tag{69}$$

In these equations all unknown components assembled in $\vec{e}$, $\dot{\vec{e}}$ and $\vec{b}$, $\dot{\vec{b}}$ are functions of the time t. In order to evaluate the fields as they develop in time we have to discretisize the time axis too. We break the time axis into equally long pieces δt. Starting - for convenience - at t = 0 we replace the time argument by an upper time index n:

$$f\,(n \cdot \delta t) = f^n. \tag{70}$$

The evaluation of $\dot{\vec{e}}$ and $\dot{\vec{b}}$ may obtained by different time integrating schemes[43] of which we will use the central difference operator:

$$\dot{f}\,(n \cdot \delta t) = \frac{1}{\delta t}\left[f\left(n \cdot \delta t + \frac{\delta t}{2}\right) - f\left(n \cdot \delta t - \frac{\delta t}{2}\right)\right] + O(\delta t^2) \tag{71}$$

or simply

$$\dot{f}^n = \left[f^{n+1/2} - f^{n-1/2}\right]/\delta t + O(\delta t^2)\ . \tag{72}$$

Applying this formula to $\dot{\vec{e}}$ yields the values of $\dot{\vec{e}}$ at integer time steps n and those of $\vec{e}$ at half time steps n + 1/2. Since $\vec{e}$ is equated to $\dot{\vec{b}}$ we need $\dot{\vec{b}}$ at half steps too.

Similarly eq. (69) equates $\vec{b}$ and $\dot{\vec{e}}$ at full time steps. We neglect here the conductivity - details see ref. 45 - and get the update form (or also called "leap frog" scheme - of Maxwell's equations:

$$\vec{b}^n = \vec{b}^{n-1} - \delta t \cdot R \cdot \vec{e}^{\,n-1/2} \tag{73}$$

$$\vec{e}^{\,n+1/2} = \vec{e}^{\,n-1/2} + \delta t\, D_\varepsilon^{-1}\,\tilde{R} \cdot \vec{b}^n + \delta t\, D_\varepsilon^{-1}\,\vec{j}^n \tag{74}$$

This set of equations now enables the calculation of the magnetic field from previous magnetic and electric fields and then the electric field from previous electric field and the just calculated magnetic field plus the driving term (given by either locally fixed time dependent currents or by charges freely moving at any speed). The matrix equations do not invoke any inversion or eigenvalue procedure but only simple multiplications (matrix times vector) at each time step.

Antenna and general scattering problems of electromagnetic waves in space represent a wide field of applications[3,46,47] but we will concentrate here on fields of moving charges. A computer code BCI has been developed[43-45] that computes self excited fields in cylindrically symmetric structures for bunches of charged particles - at any speed - passing on or off axis. The fully 3D code is currently being set up in combination with a 3D version of the eigenfrequency code URMEL.

As a typical problem - one that is hard to solve in frequency domain - we show in figure 25 the fields of a Gaussian bunch passing a bellow at the speed of light. Such graphical representations of complicated electromagnetic effects are a helpful mean for understanding and for deriving simple models[48]. The quantitative dominant elements of varying shape in an electron accelerator are the cavities. In Figure 26 we find the fields excited in three cells of the accelerating PETRA cavity[49] during one bunch passage.

The interaction between the self excited fields - the strength of which is simply proportional to the number of particles in the bunch - and the particles inside the bunch is described by the total force:

$$\vec{F}(\vec{r},\,t) = e\left[\vec{E}(\vec{r},\,t) + \vec{v}(\vec{r},\,t) \times \vec{B}(\vec{r},\,t)\right] \tag{75}$$

For high energy particles moving in z-direction at almost the speed of light we write for this wake force in a comoving particle frame describing the relative particle position $s = c_0 \cdot t - z$ in a cylindrical coordinate system:

$$\vec{F}(r,\,\varphi,\,z,\,t) = \vec{F}(r,\,\varphi,\,ct-s,\,s). \tag{76}$$

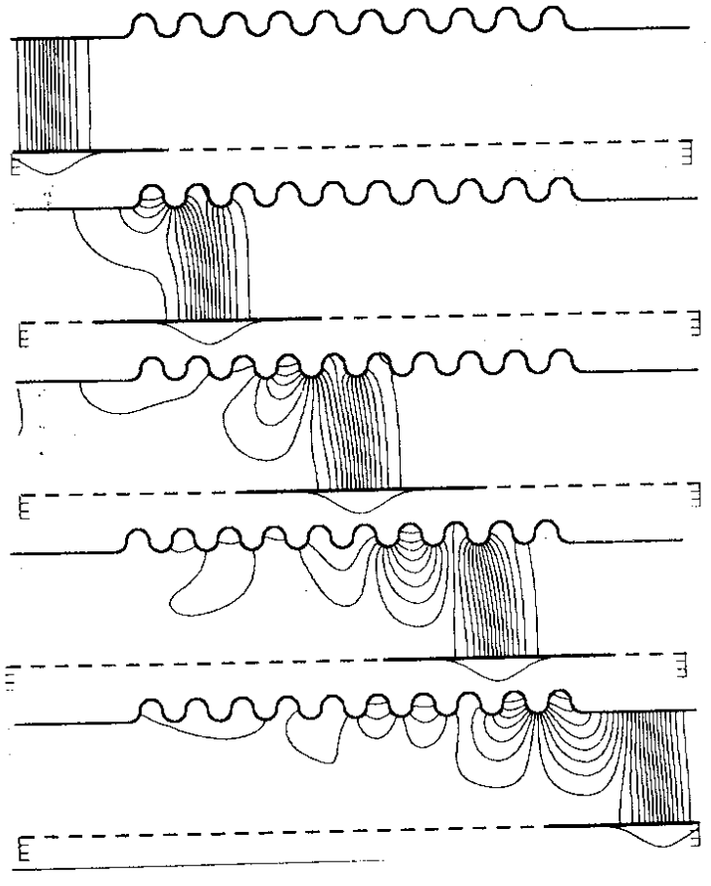

Figure 25: Electromagnetic field of a Gaussian (σ = 1 cm) bunch of charged particles traversing a bellow at the speed of light (side tube radius 6 cm, maximum radius of the bellow section 7 cm). The charge density on axis is plotted below the symmetry axis

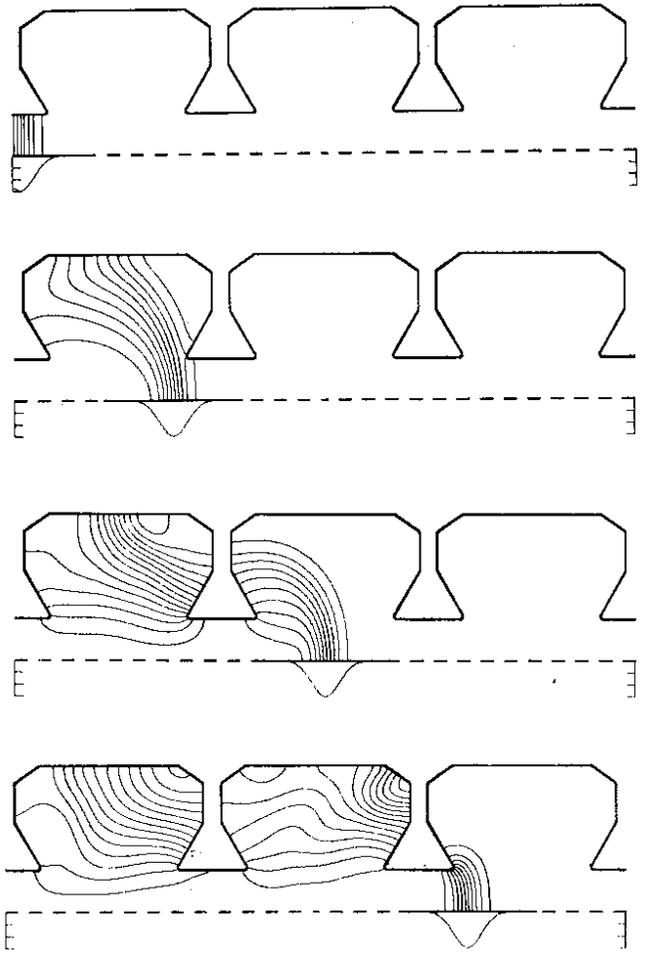

Figure 26: Electric field of a Gaussian bunch (σ = 2 cm) traversing three cells of a PETRA cavity at the speed of light. Displayed lines ($r \cdot H_\varphi$ = const) show the direction of the electric field and their density is proportional to $r \cdot |\vec{E}|$. The charge density on axis is plotted below the symmetry axis

An example of the time dependent wake force is shown in figure 27 giving the decelerating force during the passage of a bunch of a single PETRA cavity cell.

Since the time dependent force is a quickly varying function compared to the particle motion - for the case $\gamma \gg 1$ - we are mostly interested in the averaged forces after a passage of a perturbating object. These integrated forces are called wake potentials and are obtained from:

$$\vec{W}(r, \varphi, s) = \int_{-\infty}^{+\infty} \vec{F}(r, \varphi, ct-s, s)\, dt \qquad (77)$$

Integrated forces may - for resonant structures - also be obtained from a frequency analysis[50] although frequency analysis is restricted to a few specially shaped structures. For these excellent agreement has been found both theoretically[42] and numerically[51].

The effect of the self fields may be best characterized by the wake potentials as shown in figure 28. As a function of longitudinal position inside the bunch and as a function of total charge these wake potentials give the changes in momentum for each individual particle. Each value corresponds to an integral over the time dependent force as shown in figure 27.

The complementary quantity to the integrated wake force is the impedance which can be obtained by Fourier transformation. A typical result for a single PETRA cavity is shown in figure 29.

A few more integral quantities may be obtained from the wake potentials, e.g. the total energy lost by all particles and the averaged transverse kick seen by the particles.

Figure 30 shows the energy U_{cav} radiated into a PETRA cavity cell by a Gaussian bunch and the energy radiated into the exiting side tubes U_{tub}. The sum of both contributions yields the total energy U_{tot} lost by the ensemble. For short bunches it was found [52] that a significant contribution goes into the side tubes and this has two important consequences: Firstly the total energy lost is not correctly calculable by frequency codes - e.g. SUPERFISH[53] or URMEL[29] -, and - more important - secondly the interaction between the fields and the particles is no longer restricted to the cavity region but may now take place somewhere downstream the exiting side tube. By means of an analytically known dependence of the forces it is nevertheless possible to compute the total interaction in a grid only covering the cavity although physically the interaction takes place partly outside the mesh[54].The sum of all energy lost around a storage ring or along a linac is an important quantity since this energy has to be accounted for by additional accelerating voltage.

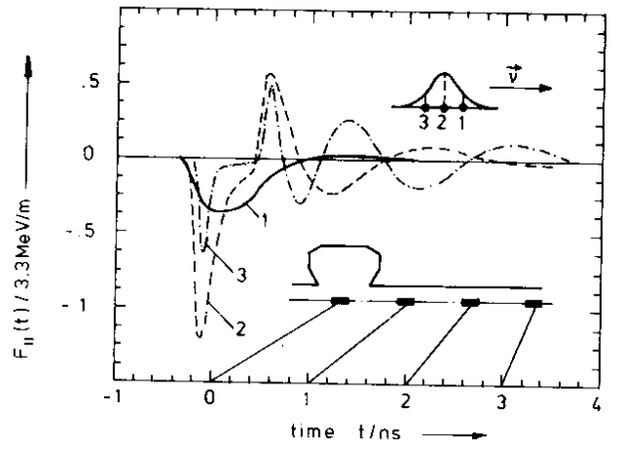

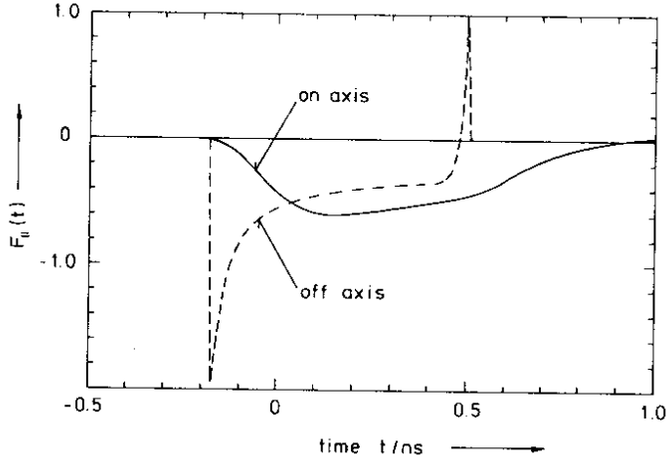

Figure 27: Time dependent decelerating wake force $F_{\parallel}(t)$ inside a Gaussian bunch (σ = 2 cm, Q = 1μC) passing a single PETRA cavity cell. At t = 0 the bunch center is in the middle of the cavity

a) $F_{\parallel}(t)$ for three test particles on axis at different longitudinal positions

b) $F_{\parallel}(t)$ for two test particles at r = 0 (on axis) and r = a (at the beam tube surface) both at the same longitudinal position (2σ ahead the center)

Note: The interaction is not limited to the cavity region (a). The integrals over $F_{\parallel}(t)$ on and off axis are identical (b).

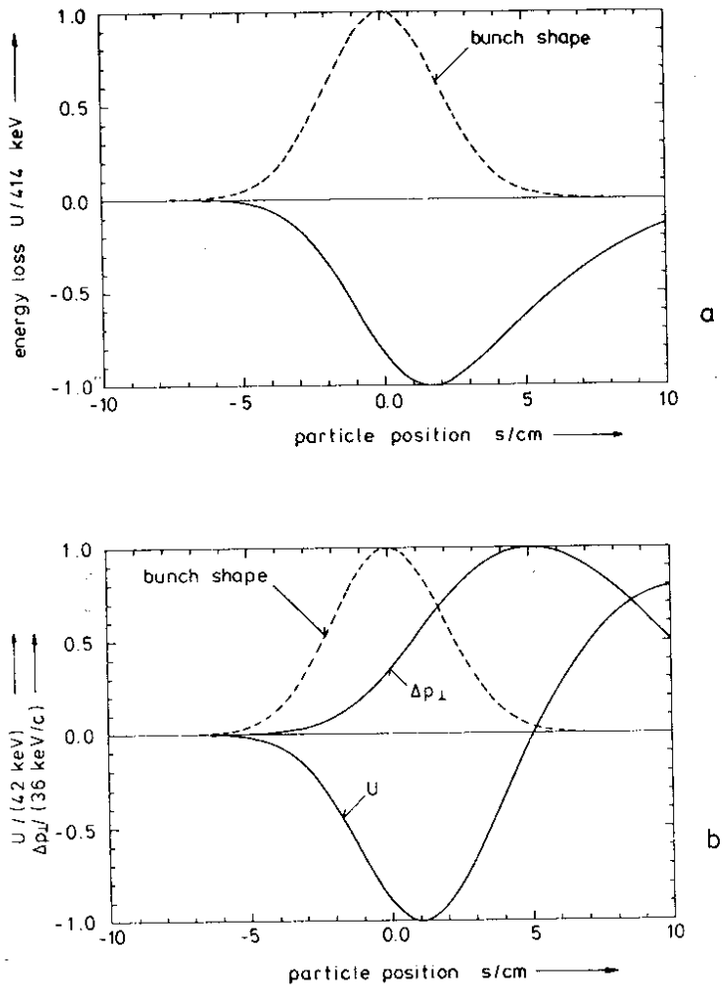

Figure 28: Integrated wake forces - called wake potentials - inside a Gaussian bunch (charge 1μC, σ = 2 cm) after the passage of a single PETRA cavity cell at a distance 0.5 cm off axis as a function of particle position (leading particles on the left)

a) energy loss U due to axis-symmetric (monopole) fields

b) energy loss U and transverse change in momentum $\Delta P_\perp$ due to dipole fields

Another measurable[55] integral quantity that may be extracted from the wake forces is the fundamental head tail mode tune shift in a storage ring[44]. In analogy to the total average loss in longitudinal momentum this gives the total transverse change in momentum averaged over all particles in the bunch. More sophisticated applications of wake forces in accelerator design are described - because of their importance - in the following separate chapter. Besides these '"parasitic" wake field effects (energy loss, deflecting forces) there are other applications of the time domain computations in the design of high gradient accelerators that rely entirely on the time character of wake forces ("wake field accelerator"[56,57]). For these structures - which are of complicated shape - computational tools are indispensible for a quantitative design.

3.5 Wake force application and collective effects
- bunch lengthening, beam instabilities -

Collective effects (bunch lengthening, head tail turbulence and beam break-up) have been found to be a major performance limitation for high energy physics devices such as SPEAR, DORIS, PETRA, PEP and the SLAC linac. Future machines are suspected of suffering even more from these effects and that is why the "a priori" study of such effects has become important during the last decade. The investigation of all collective phenomena needs as a key element the accurate knowledge of forces - or impedances in frequency domain -. (Many authors still use a single RLC resonator for modeling all these complicated electromagnetic effects around/along an accelerator). Once the forces are accurately known - by running a computer code like TBCI[43,45] - one could simply track an ensemble of superparticles using all the well known optical transfer equations and the computed self fields. A cpu time problem severly limits this approach since a field computation needs of the order of minutes and several thousand such computations are necessary.

If a Green's function could be found holding all information about the electromagnetic interaction such tracking codes could be significantly faster since the field problem has to be solved then only once and not for each interaction during the simulation. The problem is now moved to the computation of a Green's function giving the electromagnetic forces between two test particles traversing structures where fields are excited.

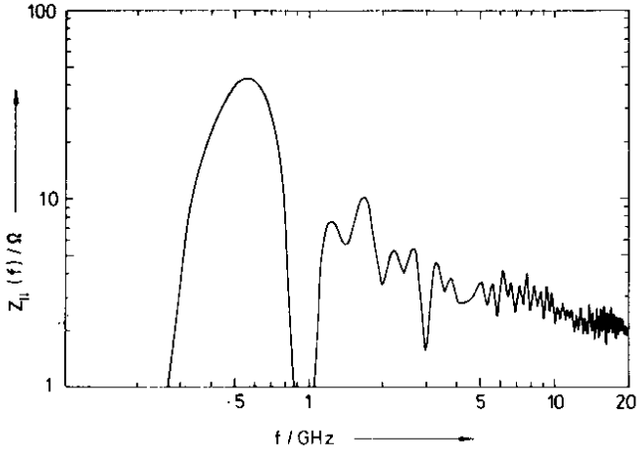

Figure 29: Real part of longitudinal impedance (Re $\{Z_{\parallel}(f)\}$) for a single PETRA cavity cell computed from the wake potential for a short Gaussian bunch (σ = 2 mm)

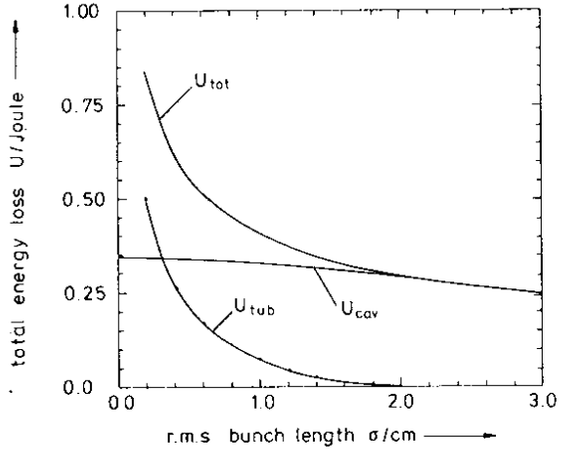

Figure 30: Energy situation after the passage of a Gaussian bunch (Q = 1μC) of a PETRA cavity cell. U_{tot} is the total energy lost by the bunch, U_{cav} is the energy radiated into the cavity, U_{tub} is the energy radiated into the side tubes

Many authors used - in the absence of computational tools - simplified models for the force such as RL, RC or RLC networks[58]. A few years ago tracking was applied to SPEAR using a Green's function derived from models that were matched with measurements[59] and the tracking results fitted the measured effects at least qualitatively. The only missing step from here to a computer program that could accurately predict such effects for any given geometry of an accelerator was the computation of forces independent of measurements. The TBCI program could almost do this job but point charges at the speed of light invoke all frequency components up to infinity at the same strength. No computer can solve such problems and the numerical approach is limited to smooth particle distributions rather than point charges.

In order to apply TBCI results we have to modify the model to a cloud of Gaussian charged balls instead of point charges. As long as the smallest ball that can be processed by TBCI is smaller than the rms extensions of the final particle distribution this approach is valid. A typical "quasi" Green's function is shown in figure 31. Such computations have been performed with a grid of over 200.000 nodes and down to bunches of rms length 2 mm traversing PETRA cavities. Such "short bunch wakes" were used for simulating bunch lengthening effects in PETRA[60].

Longitudinal particle motion in a storage ring is described by the two variables $\varepsilon = E - E_0$ (energy deviation) and τ (relative particle position with respect to some reference point). A particle transport around a storage ring lattice is simply given by:

$$\varepsilon_i^{n+1} = \varepsilon_i^n - U_{syn} \tag{78}$$

$$\tau_i^{n+1} = \tau_i^n + \alpha \frac{T_0}{E_0} \cdot \varepsilon^n \tag{79}$$

(n = turn number, i = particle number, $1 \leq i \leq I$)

When a particle traverses a cavity station its energy is changed by the rf voltage and the collective wake effects:

$$\varepsilon_i^{n+1} = \varepsilon_i^n + e\, V_{rf} \sin(\omega_{rf}\, \tau^n) + (Q_{tot}/N_{par}) \cdot e \sum_{j=1}^{I} W_{\parallel}(\tau_j^n - \tau_i^n) \tag{80}$$

Quantum excitation and radiation damping is accounted for by:

$$\varepsilon_i^{n+1} = \varepsilon_i^n - 2\varepsilon_i^n (T_0/T_\varepsilon) + 2\sqrt{T_0/T_\varepsilon} \cdot \sigma_{0\varepsilon} \cdot r \qquad (\langle r^2 \rangle = 1) \tag{81}$$

$$(\langle r \rangle = 0)$$

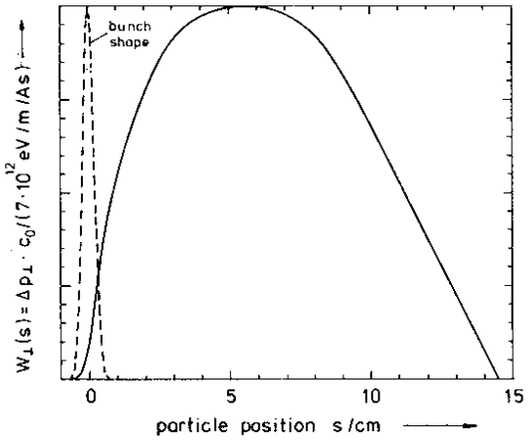

Figure 31: Typical Green's function $W_\perp(s)$ for a single PETRA cavity cell approximated by a Gaussian bunch (σ = 0.2 cm). Multiplication by the bunch offset and bunch charge yields the transverse kick on later particles at distance s from the center of the force generating bunch

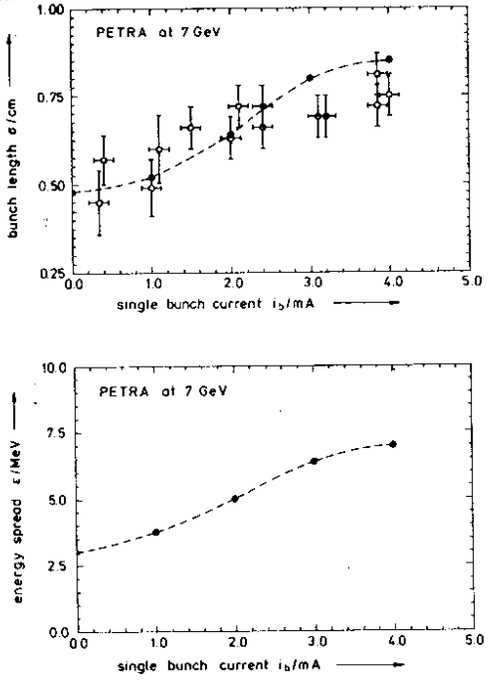

Figure 32: Bunch length (a) and energy width (b) in PETRA as a function of single beam current as calculated (●) and measured (⊢⊣) at injection energy (7 GeV) (from ref. 60)

Assembling all these equations into one set yields a relatively simple recursion formula adequate for simulation on a computer. Since the cpu time is still very costly (several thousand particles, several thousand turns) and proportional to the square of the number of particles a modified Green's function approach has been used: Instead of processing particle interactions all particles are filled into bins according to their position before they enter an rf station. The electromagmetic forces are then calculated from the bins (shape-particle interaction)[60]. This approach is an order of magnitude faster and cpu time increases only linearly with the number of particles.
Results from these calculations have been compared with beam size measurements and excellent agreement was found[60], see figure 32. Note that there is no adjustable constant in these calculations and the only necessary input are the geometrical shape of the accelerator objects and some optical properties of the storage ring.

It is particularly interesting to see how simply a long discussed problem like bunch lengthening can be solved now that the accurate forces are known.
The same technique is currently being extended for simulation of particle motion in all planes including decelerating and deflecting forces. Phase space equations for the particle motion along a lattice are well known and all one has to add is simply the transverse kick and energy change at the cavities as shown in figure 28. In the most simple approximation one may replace a superperiod of a ring by only one 4 x 4 matrix. Figure 33 shows a typical result for PETRA[61]. The so called head tail turbulence[62] is clearly found. Similar work is currently being performed in CERN[63] and Cornell University[64] using slightly different tracking equations but basically the same computer codes described here (TBCI and URMEL) for the force computation.
An attempt to provide an ultimate particle simulation code is currently being envisaged at DESY. Instead of 4 x 4 matrices for the whole storage ring an element by element tracking code RACETRACK[65] is used taking into account all the non-linearities in the optics (up to the order of dodecapole). Distributed cavity stations added to this code plus all wake forces provide a safe tool for predicting single beam current limits in future machines such as HERA, LEP and the SLC.

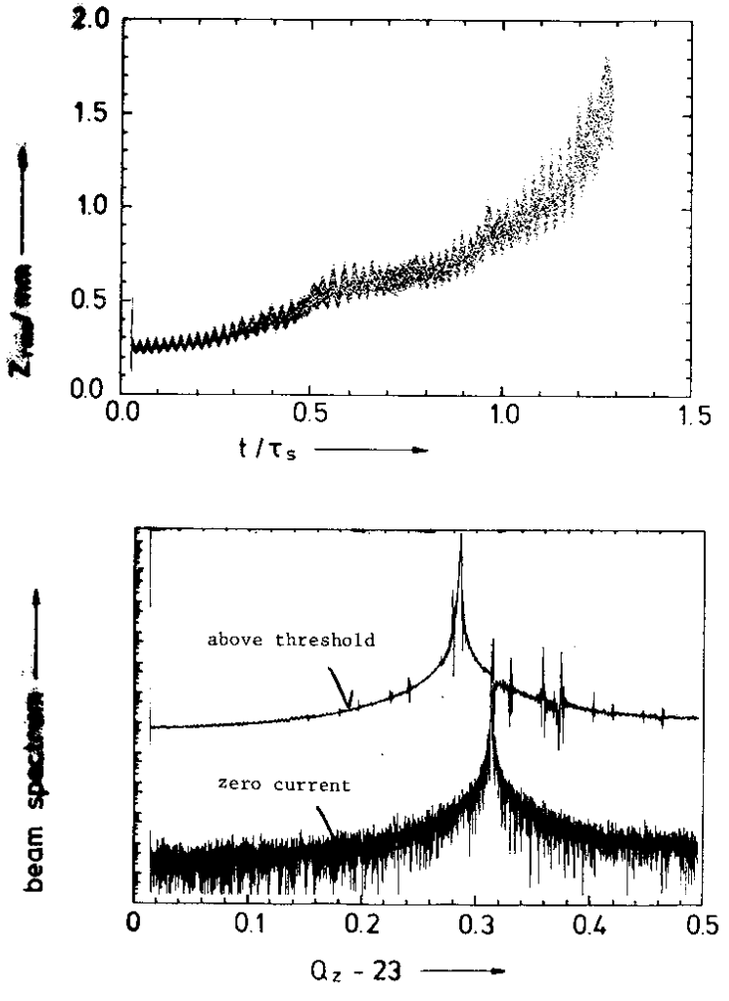

Figure 33: rms beam height in PETRA during a blow up (result from particle simulation code) and frequency spectrum of bunch motion showing indication of mode coupling

3.6 New acceleration principles

- wake field transformer, laser accelerators -

New accelerators currently being built will provide e^+e^- collisions at center of mass energies above 100-200 GeV. Storage rings for these energies must have an enormous circumference (LEP, 26 km) and larger rings for even higher energies do not seem economically feasable. Colliding linear accelerators - which do not suffer from synchrotron radiation - offer an alternative for higher energies provided they can achieve accelerating gradients over 100 MeV per meter (otherwise the size of the linacs becomes comparable to the circumference of an equivalent storage ring).

New acceleration techniques and principles have to be investigated in order to provide such high gradients. A typical application of some computer codes described in here is found in the study of near field laser accelerators[66] where guiding properties of surface waves geometries are of interest.

More recently a new principle - the wake field transformer [56] - has been published that seems to offer a realistic possibility for very high gradient accelerators in the near future.
In wake field transformers the wake field of an electron beam (or a ring) is compressed to small volumes thus generating much higher fields than those actually seen by the generating particles. By means of this principle it seems possible to make out of a 5 GeV beam with high charge a 50 GeV beam with low charge in a set up with an overall length of the order of only one kilometer. Essential for the design of such accelerators is the computation of the transient electromagnetic fields generated by relativistic particle beams in the transformer geometries. A typical ring transformer is shown in figure 34. A first experiment with a circular wake transformer is currently being prepared at DESY .

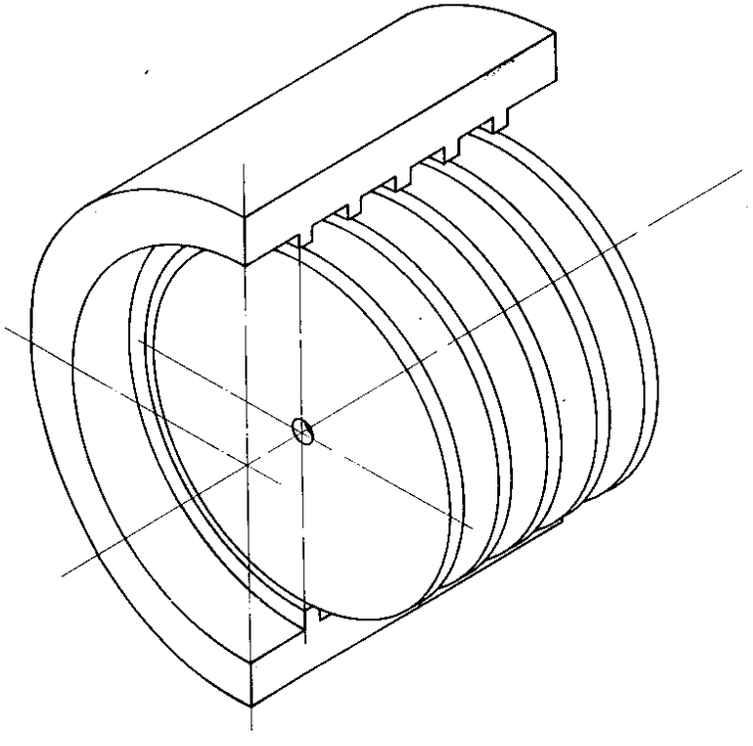

Figure 34: Cylindrical "Wake Field Transformer" with a slot for a ring charge and a center hole for a second beam. Wake fields from the ring are compressed to the center where gradients of several hundred MeV/m may be achieved

4. Summarizing remarks

A general matrix formalism has been described that allows replacement of Maxwell's equations by a set of equivalent matrix equations with a one to one correspondence. The unknowns are the electromagnetic fields just as they are in the analytical equations.

Many analytically known properties are consistently found in the grid functions when using the orthogonal dual grid approach. Applications of the matrix formalism are found whereever Maxwell's equations are valid and many examples show the universality of the method.

There is almost no restriction to the generality of geometries and material distributions. Often, complicated boundary conditions are easy accounted for in a natural way.

All the properties of the grid and the method are inductively derived from Maxwell's equations and are therefore "a priori" consistent.

5 Literature

/1/ J.C. Maxwell, Royal Society Transactions, Vol. 155, 1864

/2/ K.S. Yee, IEEE, AP-14 (1966), p. 302-307

/3/ T. Weiland, Electronics and Communication AEÜ 31 (1977), p. 116-120

/4/ W. Müller and W. Wolff, Elektrotechnische Zeitschrift ETZ-A 94 (1973), p. 276-282

/5/ W. Fritz. W. Müller and W. Wolff, Elektrotechnische Zeitschrift ETZ-A 93 (1972), p. 394-399

/6/ J. de Pablo and W. Keinstenber, Wiss. Berichte AEG-Telefunken 48 (1975), p. 158-164

/7/ W. Müller, Wiss. Berichte AEG-Telefunken 44 (1971), p. 105-109

/8/ J. de Pablo and W. Müller, Wiss. Berichte AEG-Telefunken 41 (1968), p. 17-21

/9/ J. Simkin et al., Rutherford Laboratory, RL-78-009/13, 1978

/10/ W. Müller and W. Wolff, Elektrotechnische Zeitschrift ETZ-A 96 (1975), p.269-273

/11/ D.M. Young, Trans. Am. Soc. 76 (1954), p. 92-111

/12/ H. Euler et al., Archiv für Elektrotechnik AfE 65 (1982), p. 299-307

/13/ R. Winz. Darmstädter Dissertionen D17 (Thesis), Technische Hochschule Darmstadt, FRG, 1979

/14/ A.G. Armstrong et al., Rutherford Laboratories, RL-75-066, 1975

/15/ J. Simkin and C.W. Trowbridge, RL-79-097, December 1979

/16/ T. Weiland, Archiv für Elektrische Energietechnik der etz 1 (1979), p. 263-267

/17/ T. Weiland, Archiv für Elektrotechnik AfE 60 (1978), p. 345-351

/18/ H. Euler and T. Weiland, Archiv für Elektrotechnik AfE 61 (1979), p. 103-109

/19/ H. Euler, Darmstädter Dissertation D17 (Thesis), Technische Hochschule Darmstadt, FRG, 1979

/20/ T. Weiland, The Computer Program WIMEK, Technische Hochschule Darmstadt, 1978 (unpublished)

/21/ W.A. Demerdash et al., Proc. of Intermag, Grenoble May 1981

/22/ C.S. Biddlecombe et al., Proc. Compumag Conf., Chicago 1981

/23/ W. Wolff, Proc. Compumag Conf., Oxford 1976

/24/ C.J. Carpenter and E.A. Wyatt, Proc. Compumag Conf., Oxford 1976

/25/ T.W. Preston and A.B.J. Reece, Proc. Compumag Conf., Grenoble 1978

/26/ T.W. Preston and A.B.J. Reece, Proc. Compumag Conf., Chicago 1981

/27/ C.S. Briddelcombe et al., Rutherford Laboratory, RL-81-076, p. 11-16

/28/ C.W. Trowbridge, Rutherford Laboratory, RL-81-075, 1981

/29/ T. Weiland, DESY 83-005, February 1983

/30/ T. Weiland, DESY M-82-24, October 1982

/31/ The PETRA Study Group, PETRA Proposal, DESY 1974 and 1976

/32/ H. Gerke, DESY Private Communication 1981

/33/ T. Weiland, DESY 83-##, to be published

/34/ T. Weiland, Electronics and Communication AEÜ 31 (1977), p. 308-314

/35/ T. Weiland, Electronics and Communication AEÜ 33 (1979), p. 170-174

/36/ T. Weiland, Kleinheubacher Berichte 22 (1979), p. 435-443

/37/ T. Weiland, LW-User Guide, Technische Hochschule Darmstadt, FRG, 1979, unpublished, and CERN, Computer program Library, T201, T202

/38/ PEP proposal, SLAC-189, February 1976

/39/ HERA Proposal, ECFA 80/42 and DESY-HERA 80/01, March 1980

/40/ SLC Design Report, SLAC-229, June 1980

/41/ The LEP Study Group, CERN/ISR-LEP/79-33, August 1979

/42/ T. Weiland and B. Zotter, Particle Accelerators 11 (1981), p. 143-151

/43/ T. Weiland, Proceedings of XI-th Internat. Conf on High Energy Accel., Geneva 1980, p. 570-575

/44/ T. Weiland, DESY 82-015, March 1982, also being reprinted in Nuclear Instrument and Methods, (NIM), 1983

/45/ T. Weiland, CERN/ISR-TH/80-07, January 1980
, CERN/ISR-TH/80-45, October 1980
and CERN/ISR-TH/80-46, October 1980

/46/ M.E. Brodwin, IEEE, MIT-23 (1975), p. 623-630

/47/ T. Weiland, Kleinheubacher Berichte 24 (1981), p. 37-43

/48/ K. Bane, A. Chao and T. Weiland, IEEE NS-28, No. 3, June 1981, p. 2605-2607

/49/ H. Gerke et al., DESY PET-77-08, August 1977

/50/ P.B. Wilson et sl., SLAC-Pub 1908 and PEP 240, 1977

/51/ K. Bane and T. Weiland, SLAC/AP-1, January 1983

/52/ T. Weiland, DESY M81-04, March 1981

/53/ K. Halbach and R.F. Holzinger, Particle Accelerators 7 (1976), pp. 213

/54/ T. Weiland, DESY M83-02, February 1983, accepted for publication in Nuclear Instruments and Methods (NIM), 1983)

/55/ R.D. Kohaupt and T. Weiland, DESY M82-07, April 1982

/56/ G.-A. Voss and T. Weiland, DESY 82-10. April 1982

/57/ G.-A. Voss and T. Weiland, DESY 82-074, November 1982

/58/ A. Renieri, Laboratori Nazonali di Frascati del CNEN, Report No LNF 75/11, February 1976

/59/ K. Bane, K. Satoh and P.B. Wilson, IEEE, NS-28, No. 3, June 1981, p. 2525

/60 T. Weiland, DESY 81-088, December 1981

/61/ T. Weiland and A. Wrulich, DESY 83-000, to be published

/62/ R.D. Kohaupt, DESY 80-022, March 1982

/63/ D. Brandt, CERN , private communication and CERN/ISR-TH/82-09 (1982)

/64/ R. Siemann, CBN 82-27, Cornell, 1982

/65/ A. Wrulich, DESY 83-000, To be published

/66/ T. Weiland, American Institute of Physics, AIP 91 (1982, pp. 203 and references in it and other contributions in the same volume

/67/ The Wake Field Accelerator Study Group, report to be published in the Proceedings of the XII international conference on high energy acceletors, Chicago 1983

Figure Captions

Figure 1: C-shaped dipole bending magnet (a) and course mesh for representing its cross section (b) using triangular sub cells and exploiting the symmetries

Figure 2: Double micro strip transmission line on dielectric support in a metallic rectangular waveguide (a) and course mesh representing a quarter of its cross section (b). Material (1) is dielectric, (2) vacuum and (3) may be either dielectric or metal

Figure 3: Three possible approximations to a circular shape in a mesh
a) usual "stair step" approximation
b) extended triangular sub cell approximation
c) extended triangular sub cells combined with irregular mesh steps

Figure 4: Simplest numerical approximation for one dimensional line integrals

Figure 5: Single mesh cell with four electric field components allocated around the circumference and one component of the magnetic flux density allocated to the middle of and perpendicular to the cell area

Figure 6: Three dimensional view of a mesh cell showing the magnetic flux density components evaluated at the middle of and perpendicular to the cell surface areas

Figure 7: Three (a) and two (b) dimensional examples for dual "electric" and "magnetic" grids G and $\tilde{G}$

Figure 8: Section of a 2D-mesh with several different materials (1, 2 and 3) demonstrating that only continuous components of $\vec{E}$ and $\vec{B}$ occur

Figure 9: Cell of $\tilde{G}$ for demonstration of the solution of Maxwell's second equation

Figure 10: Mesh cell of $\tilde{G}$ (a) and six electric field components allocated to the six surface areas (b)

Figure 11: Mesh cell of G with four electric field components and associated scalar potentials

Figure 12: Possible grids for approximating 2D and 3D problems
a) cells are partially filled with infinitely conducting metal in order to allow boundary conditions to be specified along curved lines
b) typical 3D (r, φ, z)-grid adequate for focussing magnets
c) combined cartesian/cylindrical grid for investigating radiation antenna problems
d) elliptical grid for 2D or 3D meshes

Figure 13: Two dimensional fully triangular grids enabling much better approximation of odd shaped structures (a) and section of a triangular grid showing cells of G with electric field components and dual hexagonal cells of $\tilde{G}$ with magnetic flux density components

Figure 14: Schematic cross section of a C-shaped bending magnet with return current and the only two components of the source field $\vec{H}_s$ in the grid that need to be nonzero

Figure 15: Magnetic flux density in a C-shaped magnet

Figure 16: Equipotential lines of a parallel plate capacitor (electrostatic deflector)

Figure 17: Structure of a 3D static matrix. The bands indicate nonzero elements. I, J and K are the numbers of grid lines in the three spatial directions. The number of rows between the elements is indicated on the right

Figure 18: Section of mesh $\tilde{G}$ used for low frequency eddy current problems. Material properties are constant in cells of $\tilde{G}$ and continuous unknowns are the magnetic (tangential) field plus the (perpendicular) current density. Scalar potentials are defined in non conducting regions and on the surface of conducting volumes

Figure 19: a) Three dimensional laminated magnet circuit with air gap and 50 Hz excitation coils
a = 8 cm; b = 8 cm; c = 16 cm; d = 15 cm; e = 2 cm; h = 2 cm; f = 50 Hz; Lamination filling factor 0.98; $\mu = 2000\mu_0$; conductivity $\gamma = 0{,}85\ 10^6\ Sm^{-1}$
b) Eddy currents and magnetic flux in a metal sheet at s = 3.5 cm from the surface at three time points. k gives the relative strength of the longest arrows

Figure 20: Azimuthal eddy current distribution in a cylindrical air coil (from ref. 19) (a = 2 cm, b = 5 cm, ℓ = 40 cm, r = 50 cm, $\gamma = 5.8\ 10^7 Sm^{-1}$, f = 50 Hz). (Only the left half is shown)
E_0 is the driving electric field.

Figure 21: Electric field of the 6-th deflecting parasitic dipole mode in the seven cell PETRA cavity at f = 1905 MHz. Only half a cell of the axially symmetric cavity is shown here.

Figure 22: Superconducting "Single Mode Cavity" (SMC) with only one single monople and dipole resonant mode
a) electric field of accelerating fundamental monopole mode
b) electric field of the TE-like dipole mode

Figure 23: Electric (a) and magnetic (b) field of the fundamental propagating wave on a micro strip transmission line on dielectric support surrounded by a rectangular waveguide (infinitely conducting). Permittivity of the dielectric is $\varepsilon = 1.5\ \varepsilon_0$ and the normalized frequency is $ak_0 = 0.16$ where a is the support thickness

Figure 24: Complex propagation constants ($\underline{k}(\omega) : \beta(\omega) - i\alpha(\omega)$) and transverse electric field of the two fundamental waves on a dielectric single material fiber waveguide. All frequencies are normalized to the support thickness a. The fibre material is defined by $\underline{\varepsilon} = 1{,}5\ \varepsilon_0(1 - i\ 0.01)$, $\mu = \mu_0$, $\gamma = 0$ and the circular waveguide is assumed to be infinitely conducting
a) propagation constants for the x and y polarized waves at $ak_0 = 7$
b) electric field of the x polarized wave
c) electric field of the y polarized wave

Figure 25: Electromagnetic field of a Gaussian ($\sigma = 1$ cm) bunch of charged particles traversing a bellow at the speed of light (side tube radius 6 cm, maximum radius of the bellow section 7 cm). The charge density on axis is plotted below the symmetry axis

Figure 26: Electric field of a Gaussian bunch ($\sigma = 2$ cm) traversing three cells of a PETRA cavity at the speed of light. Displayed lines ($r \cdot H_\varphi = \text{const}$) show the direction of the electric field and their density is proportional to $r \cdot |\vec{E}|$. The charge density on axis is plotted below the symmetry axis

Figure 27: Time dependent decelerating wake force $F_{\parallel}$ (t) inside a Gaussian bunch (σ = 2 cm, Q = 1μC) passing a single PETRA cavity cell. At t = the bunch center is in the middle of the cavity

a) $F_{\parallel}$ (t) for three test particles on axis at different longitudinal positions

b) $F_{\parallel}$ (t) for two test particles at r = 0 (on axis) and r = a (at the beam tube surface) both at the same longitudinal position (2σ ahead the center)

Note: The interaction is not limited to the cavity region (a). The integrals over $F_{\parallel}$ (t) on and off axis are identical (b)

Figure 28: Integrated wake forces - called wake potentials - inside a Gaussian bunch (charge 1μC, σ = 2 cm) after the passage of a single PETRA cavity cell at a distance 0.5 cm off axis as a function of particle position (leading particles on the left)

a) energy loss U due to axis-symmetric (monopole) fields

b) energy loss U and transverse change in momentum $\Delta P_{\perp}$ due to dipole fields

Figure 29: Real part of longitudinal impedance (Re $\{Z_{\parallel}(f)\}$) for a single PETRA cavity cell computed from the wake potential for a short Gaussian bunch (σ = 2 mm)

Figure 30: Energy situation after the passage of a Gaussian bunch (Q = 1μC) of a PETRA cavity cell. U_{tot} is the total energy lost by the bunch, U_{cav} is the energy radiated into the cavity, U_{tub} is the energy radiated into the side tubes

Figure 31: Typical Green's function $W_{\parallel}(s)$ for a single PETRA cavity cell approximated by a short Gaussian bunch (σ = 0.2 cm). Multiplication by the bunch offset and bunch charge yields the transverse kick on later particles at distance s from the center of the force generating bunch

Figure 32: Bunch length (a) and energy width (b) in PETRA as a function of single beam current as calculated (●) and measured (⊢⊣) at injection energy (7 GeV) (from ref. 60)

Figure 33: rms beam height in PETRA during a blow up (result from particle simulation code) and frequency spectrum of bunch motion showing indication of mode coupling

Figure 34: Cylindrical "Wake Field Transformer" with a slot for a ring charge and a center hole for a second beam. Wake fields from the ring are compressed to the center where gradients of several hundred MeV/m may be achieved